

Applications of Silicon-on-Insulator Photonic Crystal Structures in Miniature Spectrometer Designs

by

Boshen Gao

Submitted in Partial Fulfillment of the
Requirements for the Degree
Doctor of Philosophy

Supervised by

Professor Robert W. Boyd

The Institute of Optics
Arts, Sciences and Engineering
Edmund A. Hajim School of Engineering and Applied Sciences

University of Rochester
Rochester, New York

2017

Table of Contents

Biographical Sketch	v
Acknowledgments	viii
Abstract	xi
Contributors and Funding Sources	xiii
List of Figures	xv
List of Tables	xxiv
1 Introduction	1
1.1 A brief historical perspective	1
1.2 Photonic crystals (PCs)	5
1.3 Superprism effect in a PC	12
1.4 Defect-based PC nano-cavities and coupled-cavity waveguides (CCWs)	19

2	The design of a flat-band PC superprism	25
2.1	A quantitative analysis of the superprism effect	26
2.2	Lattice Structure Optimization	29
2.3	Finite difference time domain (FDTD) simulation of a flat-band superprism	32
3	Experimental study of a flat-band silicon superprism	35
3.1	AGD in a PC superprism	35
3.2	An 8 channel on-chip superprism spectrometer	39
4	On-chip spectroscopy with thermally tuned high-Q PC cavities	43
4.1	Optimization of an L-3 cavity for high Q	45
4.2	Thermal effect on the optical properties of nano-cavities	47
4.3	Spectrum differentiation of acetylene and hydrogen cyanide using a thermally tuned PC nano-cavity	52
5	Coupled-cavity waveguides with ultra wide-band slow-light	55
5.1	Enhancement of the spectral sensitivity of a Mach-Zehnder interferometer (MZI) by slow-light	55
5.2	Design of a wide-band slow-light coupled-cavity waveguide (CCW)	61
5.3	Experimental study of CCWs' slow-light performance	63

6	Conclusions and future works	68
----------	-------------------------------------	-----------

	Bibliography	71
--	---------------------	-----------

Biographical Sketch

The author was born in Mudanjiang, the People's Republic of China, in 1982. In 2001, he was admitted to Harbin Institute of Technology, Harbin, China. He completed his study in the Department of Applied Physics and acquired his Bachelor of Science degree in fall 2005. Advised by Professor Chunfeng Hou, the author did his undergraduate thesis research on the energy structure of electrons confined in several types of self-assembled semiconductor quantum dots. He enrolled in the PhD program at The Institute of Optics at University of Rochester in Fall 2008 and joined Professor Robert W. Boyd's research group in 2009, where he performed research studying the spectroscopic properties and applications of photonic crystal structures on silicon-on-insulator (SOI) platform.

Publications Related to This Thesis

- 1 "Design of flat-band superprism structures for on-chip spectroscopy," B. Gao, Z. Shi and R. W. Boyd, *Opt. Express* 23 (5), 6491-6496 (2015).

- 2 “On-chip spectroscopy with thermally tuned high- Q photonic crystal cavities,” A. C. Liapis, B. Gao, M. R. Siddiqui, Z. Shi and R. W. Boyd, *Appl. Phys. Lett.* 108 (2), 021105 (2016).
- 3 “Enhanced spectral sensitivity of a chip-scale photonic-crystal slow-light interferometer,” O. S. Magaña-Loaiza, B. Gao, S. A. Schulz, K. M. Awan, J. Upham, K. Dolgaleva and R. W. Boyd, *Opt. Lett.* 41 (7), 1431-1434 (2016).
- 4 “Ultra-wide-band slow light in photonic crystal coupled-cavity waveguides,” Y. Lai, M. Mohamed, B. Gao, M. Minkov, R. W. Boyd, V. Savona, R. Houdré and A. Badolato, submitted to *Nat. Photonics*.

Other Publications

- 5 “Distributed angular double-slit interference with pseudo-thermal light,” L. Gao, S. M. H. Rafsanjani, Y. Zhou, Z. Yang, O. S. Magaña-Loaiza, M. Mirhosseini, J. Zhao, B. Gao and R. W. Boyd, *Appl. Phys. Lett.* 110 (7), 071107 (2017).
- 6 “Digital spiral object identification using random light,” Z. Yang, O. S. Magana-Loaiza, M. Mirhosseini, Y. Zhou, B. Gao, L. Gao, S. M. H. Rafsanjani, G. Long and R. W. Boyd, *Light: Sci. Appl.* 6, e17013 (2017).
- 7 “Polymer encapsulated high- Q silicon photonic crystal cavities,” Y. Lai, B. Gao, M. Minkov, V. Savona, R. W. Boyd and A. Badolato, in preparation.

Conference Papers

- 1 “Slow-Light Enhanced Integrated Spectrometers on Chip,” Z. Shi, A. C. Liapis, B. Gao and R. W. Boyd, *Laser Science*, LWJ4 (2011).
- 2 “Development of a Slow-Light Spectrometer on a Chip,” S. Murugkar, I. De Leon, Z. Shi, G. Lopez-Galmiche, J. Salvail, E. Ma, B. Gao, A. C. Liapis, J. E. Vornehm and R. W. Boyd, *SPIE Photonics West OPTO*, 82640T-82640T-7 (2012).
- 3 “Applications of Photonic Crystals for Spectroscopy,” Z. Shi, A. C. Liapis, B. Gao, Y. Lai, A. Badolato and R. W. Boyd, *Laser Science*, LTh3H. 3 (2012).
- 4 “Chemical Species Discrimination by a Photonic Crystal Cavity Array,” A. C. Liapis, M. Siddiqui, B. Gao, Z. Shi and R. W. Boyd, *Frontiers in Optics*, FM4E. 4 (2013).
- 5 “Enhanced Spectral Sensitivity of a Chip-Scale Photonic-Crystal Slow-Light Interferometer,” B. Gao, O. S. Magaña-Loaiza, S. A. Schulz, K. M. Awan, J. Upham, K. Dolgaleva and R. W. Boyd, *Frontiers in Optics*, JW4A. 64 (2016).

Acknowledgments

The pursuit of one's PhD degree is just like the other parts of one's life, full of ups and downs, twists and turns. Without the support and help from many individuals, it would be a mission impossible. Upon reaching the final destination of this journey, I feel a strong urge to express my gratitude to all the colleagues and friends I have been blessed with during these years.

My journey started with an offer from Professor Robert Boyd to work in his group. I am very grateful for this opportunity. During the years, despite all sorts of challenges I encountered, Professor Boyd guided me through this journey and provided endless support, for which I will forever be indebted. He was always full of new ideas and his enthusiasm for research was endless. I also enjoyed his good sense of humor and fantastic personality.

I'm also thankful to Professor Antonio Badolato for the opportunity to collaborate on a number of projects which further developed my skill set. I would like to thank Jerry Kuper for many collaborations. I would also like to thank Professor Jaime Cardenas and Professor Gourab Ghoshal for serving on my thesis committee and

Professor Nicholas Bigelow for agreeing to be the chair. I appreciate Professor Govind Agrawal's very helpful advices on my thesis, he also served as a committee member in my thesis proposal exam.

I am very grateful to many past and present Boyd group members, both in Rochester and Ottawa: Zhimin Shi and Andreas Liapis for the numerous helpful discussions and sharing their nano-fabrication expertise; Joseph Vornehm for his enormous help in improving my writing; Sebastian Schulz for his work in our collaboration which turned my design into a real device; Jeremy Upham for his crucial suggestions on how to optimize our cross-polarization resonant scattering system; Brandon Rodenburg and Omar Magaa-Loaiza for their encouragement when I was frustrated (and the many invitations to dinners); Zhe Yang and Lu Gao for inviting me to participate in their research projects; Colin O'Sullivan, Aaron Schweinsberg, Anand Kumar Jha, Heedeuk Shin, Petros Zerom, Mehul Malik, Seyed Mohammad Hashemi Rafsanjani, Mohammad Mirhosseini, Jiapeng Zhao, Yiyu Zhou, Mahmud Siddiqui, Saumya Choudhary, Mumtaz Sheikh, Nick Black, Dongzhi Fu and many others for creating an amazing working atmosphere and their help in countless ways.

Many thanks to Kari Brick, Maria Schnitzler, Gina Kern and all the great staff members of the Institute for their assistance and support over these years.

Special thanks to Yiming Lai with whom I spent many productive hours in the lab. His experimental skills and physical insights are impressive and it was a pleasure to work with him.

Finally, I would like to thank my parents for all their hard work raising me up, and my beloved fiancée Kang Liu for being extremely supportive. Their faith in me never changed even when I had doubts about myself. Words can not sufficiently express my gratitude, but still, thank you so much!

Abstract

Optical spectroscopy is one of the most important fundamental scientific techniques. It has been widely adopted in physics, chemistry, biology, medicine and many other research fields. However, the size and weight of a spectrometer as well as the difficulty to align and maintain it have long limited spectroscopy to be a laboratory-only procedure. With the recent advancement in semiconductor electronics and photonics, miniaturized spectrometers have been introduced to complete many tasks in daily life where mobility and portability are necessary. This thesis focuses on the study of several photonic crystal (PC) nano-structures potentially suitable for miniaturized on-chip spectrometer designs.

Chapter 1 briefly introduces the concept of PCs and their band structures. By analyzing the band structure, the origin of the superprism effect is explained. Defect-based PC nano-cavities are also discussed, as well as a type of coupled cavity waveguides (CCW) composed of PC nano-cavities. Chapter 2 is devoted to the optimization of a flat-band superprism structure for spectroscopy application using numerical simulations. Chapter 3 reports a fabricated broad-band superprism and the experimental

characterization of its wavelength resolving performance. In chapter 4, the idea of composing a miniature spectrometer based on a single tunable PC nano-cavity is proposed. The rest of this chapter discusses the experimental study of this design. Chapter 5 examines the slow-light performance of a CCW and discusses its potential application in slow-light interferometry. Chapter 6 serves as a conclusion of this thesis and proposes directions for possible future work to follow up.

Contributors and Funding Sources

This work was supervised by a dissertation committee consisting of Professor Robert W. Boyd (advisor), Professor Jaime Cardenas of the Institute of Optics, University of Rochester, as well as by Professor Nicholas P. Bigelow and Professor Gourab Ghoshal of the Department of Physics and Astronomy, University of Rochester. Prof. Boyd also holds an appointment at the University of Ottawa, Ottawa, Canada.

The work described in Chapter 2 is from a published research paper co-authored by Boshen Gao, Zhimin Shi and Robert W. Boyd. Boshen Gao performed the theoretical analysis and the numerical simulations. Zhimin Shi proposed the idea of using the angular-group-dispersion-bandwidth-product (AGDBP) as a figure of merit to measure the performance of a flat-band superprism and helped organizing the structure of the paper. The superprism sample discussed in Chapter 3 was designed by Boshen Gao and fabricated by Sebastian A. Schulz. The characterization of this sample was completed by Boshen Gao in the laboratory of Prof. Antonio Badolato. The nano-cavity in the experiment described in Chapter 4 was fabricated by Andreas C. Liapids, Zhimin Shi and Boshen Gao. The characterization was performed by

Boshen Gao and Andreas C. Liapids. The CCW sample in Chapter 5 was designed by Momchil Minkov and fabricated by Yiming Lai. The characterization system was designed and built by Boshen Gao. The sample measurement and data analysis were performed by Boshen Gao.

My graduate study was primarily funded by the US Defense Threat Reduction Agency Joint Science and Technology Office for Chemical and Biological Defense (Grant No. HDTRA1-10-1-0025).

List of Figures

1.1	(a), Schematics of a Czerny-Turner miniature spectrometer. Light entering from the slit is collimated by a concave mirror before reaching the diffraction grating. Diffracted light is focused by a second concave mirror onto a detector array. (b), a crossed Czerny-Turner configuration.	2
1.2	(a), A conventional binary transmitting diffraction grating. At the n th order diffraction angle, the phase difference between light from adjacent slits is $2n\pi$. (b), Schematics of an AWG. The phase difference between light from adjacent waveguides is caused by different propagation distances.	4
1.3	Schematics of an 1-D (a), 2-D (b) and 3-D (c) photonic crystals. . . .	6
1.4	(a), Schematics of a 2-D square lattice PC. $\mathbf{a}_1 = a\hat{\mathbf{x}}$ and $\mathbf{a}_2 = a\hat{\mathbf{y}}$ are the two primitive lattice vectors. (b), The corresponding reciprocal lattice and primitive vectors. $ \mathbf{b}_1 = \mathbf{b}_2 = 2\pi/a$. The red area shows the first Brillouin zone.	9

- 1.5 (a), Refraction of light at the interface between a dielectric medium and vacuum. The refractive index of the dielectric medium is $n = 1.5$. (b), an analysis of the refraction using EFCs. The EFCs of vacuum and the medium are plotted in the k space, separated by the k_x axis. \mathbf{k}_1 and \mathbf{k}_2 are the wave vectors in vacuum and the dielectric medium, respectively. To obtain \mathbf{k}_2 from \mathbf{k}_1 , note that the conservation of energy requires that $\omega_2 = \omega_1$. On the other hand, the boundary conditions state that $k_{x2} = k_{x1}$. It follows that a dashed line $k_x = k_{x1}$ intersects the EFC $\omega_2 = \omega_1$ at a point which is the end point of \mathbf{k}_2 14
- 1.6 (a), Schematic diagram of a 2-D PC slab with a square lattice; (b), the EFCs of the PC in the first Brillouin zone; (c), the EFCs of an isotropic bulk medium. Two beams with wave vectors \mathbf{k}_1 and \mathbf{k}_2 propagate along the directions of their group velocities \mathbf{v}_1 and \mathbf{v}_2 , respectively. Since the EFCs are concentric circles, the group velocity of either beam is collinear with the wave vector of the beam. (d), superprism effect of beams with different incidence angles. Inside the PC region, the group velocity of a beam is no longer collinear with the Bloch wave vector. The directions of \mathbf{v}_1 and \mathbf{v}_2 differ by a larger amount than those of \mathbf{k}_1 and \mathbf{k}_2 do. (e), superprism effect of beams with different frequencies. 16

- 1.7 Negative diffraction. (a), a beam of finite size propagating along the z direction from plane A to plane B. Its angular spectrum contains a continuum of \mathbf{k} vectors centering on \mathbf{k}_0 . (b), the EFCs of an isotropic bulk medium. Since the EFCs are concave, $\mathbf{k}_{1z} - \mathbf{k}_0 < 0$ for $\mathbf{k}_1 \neq \mathbf{k}_0$. (c), EFCs of a PC. In the region where the contour is a convex curve, $\mathbf{k}_{1z} - \mathbf{k}_0 > 0$ for $\mathbf{k}_1 \neq \mathbf{k}_0$ is true. (d), the result of a FDTD simulation showing the effect of negative diffraction. A beam is preconditioned by free propagation in the bulk medium before it enters the PC area. Inside the PC area, the beam is focused again due to the negative diffraction. 18
- 1.8 (a), An L-3 cavity. Three air holes are removed from a hexagonal lattice PC. (b), the electric field profile (E_y) of the fundamental resonant mode. The mode is confined by Bragg reflection in all directions in the PC plane. (c), a coupled-cavity waveguide (CCW) composed of a series of L-3 cavities. The distance between neighboring cavities is $\Lambda = 2\sqrt{3}a$ where “ a ” is the lattice constant of the PC. (d), dispersion profile predicted by the tight-binding approximation. Only effects from the nearest neighbors are considered. (e), group index as a function of frequency. Near the center frequency ω_0 , the curve shows a uniform behavior. 21

- 2.1 Equi-frequency contours (EFCs) of a 2-D square lattice PC in the first Brillouin zone. The light beam enters the PC region at an incidence angle α_{inc} and the “refraction” angle inside the PC region is labeled as α_{pc} . Solid arrows are the Bloch \mathbf{k} vectors which also represent the direction of phase velocities of the beams. Dashed arrows are normal to the EFC contour, indicating the directions of group velocities. Strong anisotropy leads to deviations of the EFCs from perfect circles. Near the band edge in k -space, a small change in frequency leads to a large directional variation in group velocity. Inset: the PC structure in real space. \mathbf{a}_1 and \mathbf{a}_2 are the two primitive lattice vectors. The radius of the air holes is $r = 0.3a$ where $a = |\mathbf{a}_1|$ is the lattice constant. 27
- 2.2 Geometric analysis of beam propagation in a general 2-D PC. (a), the PC structure in coordinate space; θ and d are the two adjustable parameters; (b), corresponding reciprocal lattice; \mathbf{k}_1 is perpendicular to \mathbf{a}_1 and \mathbf{k}_2 to \mathbf{a}_2 . (c), EFC plot of the structure. The k_x axis is chosen to be along the \mathbf{k}_2 direction. 30

2.3 Optimization results for obtaining a flat-band PC superprism. (a), Maximum value of the angular-group-dispersion bandwidth product (AGDBP) \mathcal{P}_{\max} as a function of position in the two dimensional parameter space; (b), Superprism factor q as a function of the normalized frequency ω plotted for 3 structures: ① $\mathcal{P}_{\max} = 0.839$ rad, $d = 0.9a_1$, $\theta = 89^\circ$; ② $\mathcal{P}_{\max} = 0.802$ rad, $d = 0.9a_1$, $\theta = 83^\circ$; ③ $\mathcal{P}_{\max} = 0.809$ rad, $d = 1.1a_1$, $\theta = 88^\circ$ 31

2.4 (a) Schematic diagram of a flat-band superprism spectrometer; (b) spectral transmission of the 8 channels that are evenly spaced over the working bandwidth. 33

3.1 (a), Maximum value of the AGDBP \mathcal{P}_{\max} as a function of position in the two dimensional parameter space; (b), the lattice of the PC; (c), schematic diagram of the superprism structure. 36

3.2 (a), End-fire coupling system; (b), an image of the scattering trench and part of the PC region under infrared illumination. The x direction is defined as shown. Scale bar is displayed at the bottom right corner. (c), light scattered from the trench; (d), spot position along the x axis versus input wavelength. 38

3.3 (a), Schematic diagram of an 8 channel superprism spectrometer; (b), image of eight single-mode output waveguides; (c), the spectral flux transmission measured at the end of eight output waveguides. 40

3.4	Spectral flux transmission from 6 channels. The maximum inter-channel crosstalk is -4.2 dB induced by channel 3 in channel 5.	41
4.1	Operating principle of a PC cavity spectrometer using (a) an array of sequentially tuned cavities or (b) a single dynamically-tunable cavity.	44
4.2	(a) Schematics of an intrinsic L-3 cavity and the electric field profile (E_y) of the fundamental resonant mode. The simulated Q factor is 4701. (b) The E -field distribution along the x -axis; (c) Spatial Fourier transform of the E -field in (b). Dashed lines show the boundary of the region where $ k < \frac{2\pi}{\lambda_0}$ and λ_0 is the wavelength of light in vacuum. . .	45
4.3	(a) Schematics of an L-3 cavity with the inner two air holes moved outward by an amount of $0.15a$. In the Fourier domain, less light falls into the leaky zone. The simulated Q factor is 38430. (b) The two inner holes are moved by $0.164a$ and their radii are reduced to $0.214a$. The simulated Q factor is 97646, more than 20 times higher than the intrinsic L-3 cavity.	48

- 4.4 (a) Scanning-electron micrograph of an L-3 PC cavity optimized for vertical out-coupling. The holes are labeled according to their design radii. In this example, $r_1 = 89$ nm, $r_2 = 93$ nm, $r_3 = 62$ nm. Additionally, the holes labeled “3” are shifted outwards by 62 nm. (b) Schematic of the setup used to characterize PC cavities via resonant scattering. P1 and P2: crossed polarizers, $\lambda/2$: half-wave plate. Note that the light incident on the PC cavity is x-polarized, and that only light that is y-polarized is being collected by the detector. (c) Measured resonance of a typical L-3 PC cavity, displaying a Q of $\sim 6.7 \times 10^3$ 49
- 4.5 (a), Resonance peaks of the fabricated L-3 cavity at different temperatures; (b) Resonant wavelength versus temperature. The linear fit gives an estimated slope of 0.07 nm/°C. A tuning range of 1.4 nm is demonstrated. (c) Q factor at different temperatures and (d), coupling efficiency η as functions of temperature. 51
- 4.6 (a), Schematic of the setup used for spectroscopic measurements. (b), Measured transmission spectra of the hydrogen cyanide (top) and acetylene (bottom) gas cells. The transmission of the two gas cells, measured using a tunable laser, is also shown (solid lines). Note that the spectral resolution is adequate to discriminate between the two gases. 53

5.1	(a), Schematics of a MZI with an arm length difference of L and the transmittance as a function of frequency; (b), A slow-light material is inserted in one arm of the MZI. The transmittance profile shows a spectral sensitivity enhanced by a factor of the group index of the slow-light material.	56
5.2	(a), Scanning electron microscope (SEM) photograph of the fabricated PC waveguides with its input channel; (b), Fiber based MZI containing a PC slow-light waveguide in one of the arms; (c), Interference fringes as a function of wavelength measured by the OSA; (d)-(f), Three different 1 nm spans with significantly different fringe spacings.	59
5.3	Experimental measurements and theoretical predictions of the density of interference fringes plotted as a function of wavelength for the slow-light MZ interferometer of Fig. 5.2(b). The green curve is the simulated fringe density of the MZI when the slow-light waveguide is replaced by free space of the same length.	60
5.4	(a), Schematic diagram of the CCW design. (b), SEM top view picture of a 50-CCW. Red arrows indicate the input and output of light in the PC waveguides.	62
5.5	(a), Schematics of the experiment setup. (b), Normalized transmitted intensity as a function of laser frequency. (c), Relative phase change calculated from (b).	65

5.6	(a), Normalized transmitted intensity when there is no CCW, a 400-CCW and a 800-CCW in the MZI, respectively.(b), Relative phase calculated from (a). (c),(d), Transmission profiles of the CCWs. (e),(f), Group indices of the CCWs as a function of wavelength calculated from equation 5.7. The noise is mainly due to laser sweeping wavelength error.	66
6.1	(a), Specially engineered interface hole shape for high efficiency coupling. (b), Adiabatic transition of hole radii near the edge of the PC area.	70

List of Tables

3.1	Comparison between several types of on-chip compact spectrometers. $\delta\lambda$: spectral resolution. N : number of resolvable channels. *: the nanocavities array requires additional vertical out-coupling setup for far-field emission detection. **: the disordered photonic chip design re- lies on computational methods to extract the spectral information from measured signals, thus additional computer hardware and software are necessary.	42
-----	---	----

1 Introduction

1.1 A brief historical perspective

The beginning of spectroscopy dated back to the 1600s when Isaac Newton conducted his famous experiments on light's dispersion through a prism. In his book *Opticks* [1], Newton first applied the word "*spectrum*" to describe the rainbow of colors generated by sun light passing through a glass prism, which can be considered as the earliest form of a "spectrometer". Joseph Fraunhofer developed the first prism spectroscope in the year of 1814. Even in modern days, prism spectroscopes are still found in use for education purpose in various circumstances. He later replaced the prism with a diffraction grating which enhanced the spectral resolution of a spectroscope and made the measurement of absolute wavelength possible. Since then, spectroscopy has evolved into a complicated and systematic methodology for modern scientific researches. Along its evolution, the spectrometers have also taken various forms:

prisms, gratings, or interferometers, etc. While advanced high-resolution table top spectrometers play an important role in many laboratories today, they are often bulky and difficult to maintain for out-of-lab usage, e.g., real time chemical identification in battle fields, drug and explosive detections in airports, fast analysis of possible air pollutions at a fire scene, or in wearable medical devices and smart devices, etc. These applications demand the miniaturization of spectrometers.

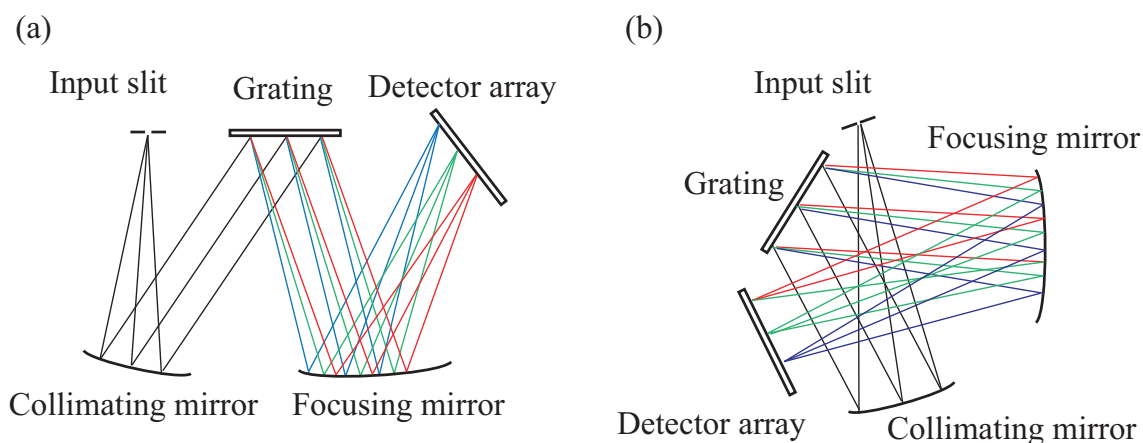


Figure 1.1: (a), Schematics of a Czerny-Turner miniature spectrometer. Light entering from the slit is collimated by a concave mirror before reaching the diffraction grating. Diffracted light is focused by a second concave mirror onto a detector array. (b), a crossed Czerny-Turner configuration.

Many early miniature spectrometers are simply scaled down from their classical table top counterparts to achieve portability at a cost of resolutions. One example is the Czerny-Turner configuration spectrometer [2] as shown in Fig. 1.1(a), where the miniaturization is achieved by folding the optical path through reflections by mirrors. This type of miniature spectrometer relies on a diffraction grating to work and requires

a certain free propagation distance of the light since collimation of the beam and focusing are needed. The size of such a device is limited by the radii of the mirrors and the area of the grating: if the mirrors and the grating are too small, the performance deteriorates due to the diffraction at these small apertures [3]. The dimension of a Czerny-Turner miniature spectrometer is typically of the order of 10 cm. The form factor can be further reduced by adopting the crossed Czerny-Turner configuration as shown in Fig. 1.1(b), but the weight of the device does not reduce by much since it contains the same number of optical elements. For outer space applications, cost is directly related to the weight of the cargo a rocket carries. In addition, weight is also an important factor for the design of wearable medical devices and consumer electronic products with spectroscopy functions. Thus, further miniaturizations of a spectrometer is desirable. Thanks to the advancement in semiconductor fabrication technology and nano-photonics, various types of on-chip integrated spectrometers are developed in recent decades [4–14]. One of the most widely used configuration is the arrayed waveguide grating (AWG) [5, 6, 13, 14] spectrometer, the schematics of which is shown in Fig. 1.2. When light is incident on a conventional grating at an angle “ θ_i ”, the n th order diffraction occurs when the phase difference between light from adjacent slits/reflectors is $2n\pi$ and “ n ” is an integer. The diffraction angle “ θ_n ” can be determined from the grating equation:

$$d(\sin \theta_i + \sin \theta_n) = n\lambda \quad (1.1)$$

where λ is the wavelength of light in vacuum. In an AWG, the phase difference

is produced by the different lengths of the waveguides which are fabricated using high index materials. The lengths of the waveguides are typically of the order of several millimeters. This type of design eliminates the need for collimation/focusing optics since light is always guided inside waveguides. Moreover, AWGs fabricated on semiconductor chips can be readily integrated into large scale photonic circuits and electronic products.

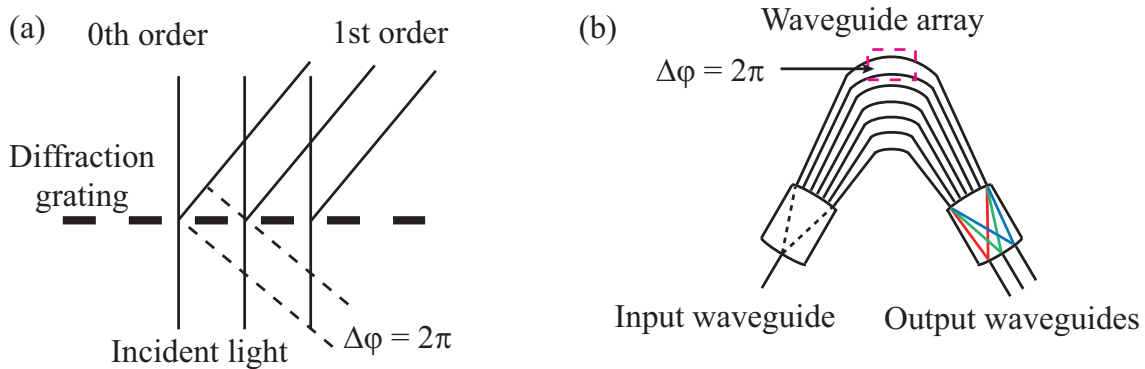


Figure 1.2: (a), A conventional binary transmitting diffraction grating. At the n th order diffraction angle, the phase difference between light from adjacent slits is $2n\pi$. (b), Schematics of an AWG. The phase difference between light from adjacent waveguides is caused by different propagation distances.

Another intriguing candidate for the miniaturization of spectrometers are the photonic crystals (PCs) [15–22]. Due to their unique optical properties and small footprint, PCs provide one more possible approach to tackle this problem. The purpose of this thesis is to report my research works on PC superprism and PC nano-cavity structures and their applications in miniature spectrometer designs. The details of

PC structures' optical properties are introduced in the next section.

1.2 Photonic crystals (PCs)

1.2.1 General background

Photonic crystals (PCs) are periodic dielectric patterns with feature sizes comparable to the wavelength of light. Such a strong modulation of the dielectric constant within the medium results in banded features in the dispersion relation of a PC, much like what a real crystal does to an electron giving rise to the electronic energy bands. Only light within certain frequency bands can propagate inside a PC. Between the bands, there are the photonic band gaps [23–25].

There are many naturally occurring PCs, for example, the colorful wings of butterflies, the iridescent feathers of peacocks or the beautiful opals found in rings, necklaces and earrings. Lord Rayleigh did the first studies on the propagation of electromagnetic waves in one-dimensional periodic dielectric stacks in 1887 [26]. In 1987, Eli Yablonovitch and Sajeev John [16, 17] adopted the word “crystal” in their work to describe 3-D periodic dielectric structures. In 1989, the name “photonic crystal” was formally introduced by Yablonovitch in his work *“Photonic band structure: The face-centered-cubic case”* [27].

Depending on the dimensionality of the periodicity, there are 1-D, 2-D and 3-D PCs as shown in Fig. 1.3 One example of a 1-D PC is a multilayer thin film stack

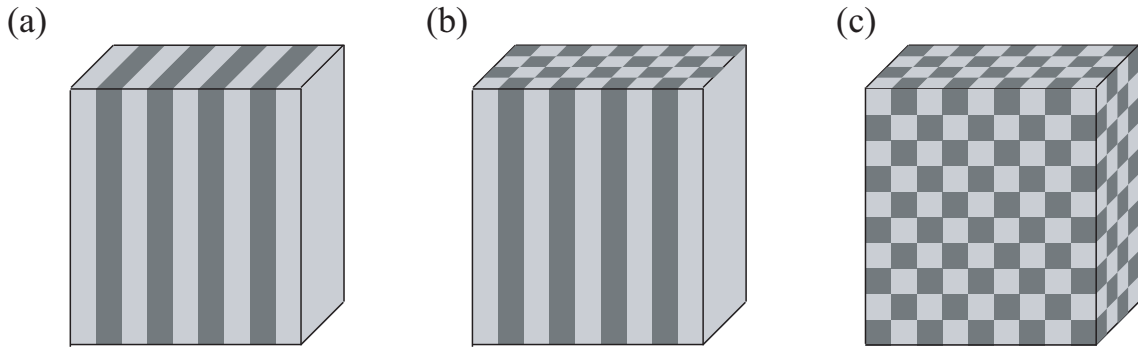


Figure 1.3: Schematics of an 1-D (a), 2-D (b) and 3-D (c) photonic crystals.

which is widely used in the making of Bragg mirrors. The high-reflectivity wavelength region of such a mirror is the band gap of the 1-D PC.

A 2-D PC has more intriguing optical properties due to the increase in the dimensionality. The most common form of a 2-D PC studied in literatures is PC slabs. A PC slab is composed of a piece of dielectric slab with a periodic pattern of air holes etched through the slab. The air holes provide a 2-D periodic modulation of the dielectric constant in the plane and supported modes are confined by index guiding in the third direction. Near the photonic band edge of a 2-D PC, the dispersion relation of light can differ significantly from that of a homogeneous medium. Such an effect can lead to many unconventional optical properties, e.g., negative refraction [28–34], self-collimation [35, 36], superprism effect [37–40], etc. Although these effects can be observed in 3-D PCs, the fabrication procedure of 3-D PC structures proves to be considerably more challenging than that of a 2-D PC [41, 42], while the addition of a third dimension does not benefit all applications. In this thesis, all the work are done in silicon 2-D PC slabs.

1.2.2 Maxwell equations in PCs

To better describe the propagation of light in the PCs, we introduce a brief theoretical discussion in this section. The behavior of light in dielectric materials is governed by the Maxwell equations [43]:

$$\begin{aligned}
 \nabla \cdot \mathbf{D}(\mathbf{r}, t) &= \rho(\mathbf{r}, t) \\
 \nabla \times \mathbf{H}(\mathbf{r}, t) - \frac{\partial \mathbf{D}(\mathbf{r}, t)}{\partial t} &= \mathbf{J}(\mathbf{r}, t) \\
 \nabla \times \mathbf{E}(\mathbf{r}, t) + \frac{\partial \mathbf{B}(\mathbf{r}, t)}{\partial t} &= 0 \\
 \nabla \cdot \mathbf{B}(\mathbf{r}, t) &= 0.
 \end{aligned} \tag{1.2}$$

The electric field $\mathbf{E}(\mathbf{r}, t)$ and the electric displacement field $\mathbf{D}(\mathbf{r}, t)$ are related by:

$$\mathbf{D}(\mathbf{r}, t) = \epsilon(\mathbf{r}, t)\epsilon_0\mathbf{E}(\mathbf{r}, t), \tag{1.3}$$

where $\epsilon(\mathbf{r}, t)$ is the dielectric constant distribution in the PC, $\epsilon_0 = 8.85 \times 10^{-12}$ F/m is the vacuum permittivity. Similarly, the magnetic induction field $\mathbf{B}(\mathbf{r}, t)$ and the magnetic field $\mathbf{H}(\mathbf{r}, t)$ are related by:

$$\mathbf{H}(\mathbf{r}, t) = \mu(\mathbf{r}, t)\mu_0\mathbf{B}(\mathbf{r}, t), \tag{1.4}$$

where $\mu(\mathbf{r}, t)$ is the relative permeability and $\mu_0 = 4\pi \times 10^{-7}$ H/m the vacuum permeability. The physical quantities $\rho(\mathbf{r}, t)$ and $\mathbf{J}(\mathbf{r}, t)$ are the free charge and electric current densities. We assume that the PC is composed of dielectric materials which do not change over time, then $\epsilon(\mathbf{r}, t)$, $\mu(\mathbf{r}, t)$ are reduced to $\epsilon(\mathbf{r})$, $\mu(\mathbf{r})$. In addition, most PC structures are fabricated from materials with a relative permeability close

to unity. Therefore, it is reasonable to assume that $\mu(\mathbf{r}) = 1$. We also assume there are no charges and electric currents in the PC, i.e., $\rho(\mathbf{r}, t) = 0$, $\mathbf{J}(\mathbf{r}, t) = 0$. Under these assumptions, Eq. 1.2, 1.3, 1.4 can be rewritten as:

$$\begin{aligned}\nabla \cdot [\epsilon(\mathbf{r})\mathbf{E}(\mathbf{r}, t)] &= 0 \\ \nabla \times \mathbf{H}(\mathbf{r}, t) - \epsilon(\mathbf{r})\epsilon_0 \frac{\partial \mathbf{E}(\mathbf{r}, t)}{\partial t} &= 0 \\ \nabla \times \mathbf{E}(\mathbf{r}, t) + \mu_0 \frac{\partial \mathbf{H}(\mathbf{r}, t)}{\partial t} &= 0 \\ \nabla \cdot \mathbf{H}(\mathbf{r}, t) &= 0.\end{aligned}\tag{1.5}$$

Writing the electric and magnetic fields in their harmonic modes:

$$\mathbf{E}(\mathbf{r}, t) = \mathbf{E}(\mathbf{r}) \exp(-i\omega t),\tag{1.6}$$

$$\mathbf{H}(\mathbf{r}, t) = \mathbf{H}(\mathbf{r}) \exp(-i\omega t),\tag{1.7}$$

the two curl equations in Eq. 1.5 become:

$$\nabla \times \mathbf{H}(\mathbf{r}) = -i\omega\epsilon_0\epsilon(\mathbf{r})\mathbf{E}(\mathbf{r}),\tag{1.8}$$

$$\nabla \times \mathbf{E}(\mathbf{r}) = i\omega\mu_0\mathbf{H}(\mathbf{r}).\tag{1.9}$$

Divide both sides of Eq. 1.8 by $\epsilon(\mathbf{r})$ and take the curl, then substitute Eq. 1.9 into it, we have:

$$\nabla \times \left(\frac{1}{\epsilon(\mathbf{r})} \nabla \times \mathbf{H}(\mathbf{r}) \right) = \left(\frac{\omega}{c} \right)^2 \mathbf{H}(\mathbf{r}).\tag{1.10}$$

If we define an operator $\hat{\Theta}$ as:

$$\hat{\Theta} = \nabla \times \left(\frac{1}{\epsilon(\mathbf{r})} \nabla \times \right),\tag{1.11}$$

Eq. 1.10 turns into:

$$\hat{\Theta}\mathbf{H}(\mathbf{r}) = \left(\frac{\omega}{c}\right)^2 \mathbf{H}(\mathbf{r}). \quad (1.12)$$

This is an eigenvalue problem, where $\mathbf{H}(\mathbf{r})$ is the eigenfunction with an eigenvalue of $(\omega/c)^2$. Generally speaking, there are no analytical solutions to this equation in a PC structure and computer aided numerical methods are used to seek $\mathbf{H}(\mathbf{r})$ [44].

1.2.3 Bloch theorem

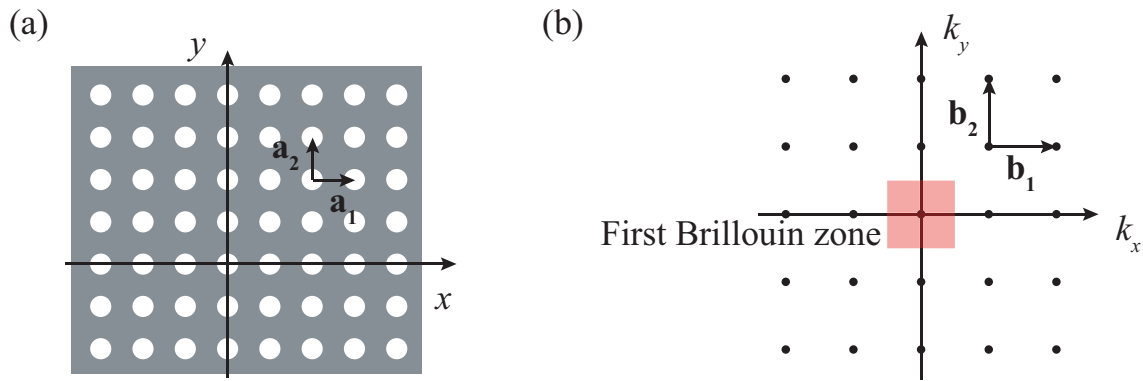


Figure 1.4: (a), Schematics of a 2-D square lattice PC. $\mathbf{a}_1 = a\hat{x}$ and $\mathbf{a}_2 = a\hat{y}$ are the two primitive lattice vectors. (b), The corresponding reciprocal lattice and primitive vectors. $|\mathbf{b}_1| = |\mathbf{b}_2| = 2\pi/a$. The red area shows the first Brillouin zone.

Figure 1.4(a) shows a 2-D square lattice PC where $\mathbf{a}_1 = a\hat{x}$ and $\mathbf{a}_2 = a\hat{y}$ are the two primitive lattice vectors. The corresponding reciprocal lattice in the k -space is

shown in Fig. 1.4(b), with the two reciprocal vectors defined as:

$$\begin{aligned}\mathbf{b}_1 &= \frac{2\pi}{a} \hat{\mathbf{x}} \\ \mathbf{b}_2 &= \frac{2\pi}{a} \hat{\mathbf{y}}.\end{aligned}\tag{1.13}$$

The dielectric constant is periodic in the two directions of \mathbf{a}_1 and \mathbf{a}_2 . Consequently, if the PC is shifted along a vector

$$\mathbf{R} = m\mathbf{a}_1 + n\mathbf{a}_2\tag{1.14}$$

where “ m ” and “ n ” are integers, it is still the same structure. Define a translation operator $\hat{\mathbf{T}}_{\mathbf{r}}$ that shifts a function by \mathbf{r} , i.e., $\hat{\mathbf{T}}_{\mathbf{r}}f(\mathbf{r}_0) = f(\mathbf{r}_0 - \mathbf{r})$ the above statement can be mathematically expressed as:

$$\hat{\mathbf{T}}_{\mathbf{R}}\epsilon(\mathbf{r}) = \epsilon(\mathbf{r} - \mathbf{R}) = \epsilon(\mathbf{r}).\tag{1.15}$$

It can be shown that a plane wave $\exp(i\mathbf{k} \cdot \mathbf{r})$ is an eigenfunction of $\hat{\mathbf{T}}_{\mathbf{R}}$ with an eigenvalue $\exp(-i\mathbf{k} \cdot \mathbf{R})$:

$$\hat{\mathbf{T}}_{\mathbf{R}} \exp(i\mathbf{k} \cdot \mathbf{r}) = \exp[i\mathbf{k} \cdot (\mathbf{r} - \mathbf{R})] = \exp(-i\mathbf{k} \cdot \mathbf{R}) \exp(i\mathbf{k} \cdot \mathbf{r}).\tag{1.16}$$

Note that for any plane waves with wave vectors of $\mathbf{k}' = \mathbf{k} + l\mathbf{b}_1 + p\mathbf{b}_2$ where l, p are integers, the eigenvalue is the same:

$$\begin{aligned}\hat{\mathbf{T}}_{\mathbf{R}} \exp(i\mathbf{k}' \cdot \mathbf{r}) &= \exp(-i\mathbf{k}' \cdot \mathbf{R}) \exp(i\mathbf{k}' \cdot \mathbf{r}) \\ &= \exp(-i\mathbf{k} \cdot \mathbf{R}) \exp(-2lm\pi i - 2np\pi i) \exp(i\mathbf{k}' \cdot \mathbf{r}) \\ &= \exp(-i\mathbf{k} \cdot \mathbf{R}) \exp(i\mathbf{k}' \cdot \mathbf{r})\end{aligned}\tag{1.17}$$

due to the definition of \mathbf{b}_1 and \mathbf{b}_2 . Moreover, the operators $\hat{\mathbf{T}}_{\mathbf{R}}$ and $\hat{\Theta}$ commute, that is, $[\hat{\mathbf{T}}_{\mathbf{R}}, \hat{\Theta}] = 0$, or

$$\hat{\mathbf{T}}_{\mathbf{R}}^{-1} \hat{\Theta} \hat{\mathbf{T}}_{\mathbf{R}} = \hat{\Theta}. \quad (1.18)$$

This can be proved by applying the left side of Eq. 1.18 on an eigenfunction $\mathbf{H}(\mathbf{r})$ of $\hat{\Theta}$:

$$\begin{aligned} \hat{\mathbf{T}}_{\mathbf{R}}^{-1} \hat{\Theta} \hat{\mathbf{T}}_{\mathbf{R}} \mathbf{H}(\mathbf{r}) &= \hat{\mathbf{T}}_{\mathbf{R}}^{-1} \hat{\Theta} \mathbf{H}(\mathbf{r} - \mathbf{R}) \\ &= \hat{\mathbf{T}}_{\mathbf{R}}^{-1} \nabla \times \left(\frac{1}{\epsilon(\mathbf{r})} \nabla \times \mathbf{H}(\mathbf{r} - \mathbf{R}) \right) \\ &= \nabla \times \left(\frac{1}{\epsilon(\mathbf{r} + \mathbf{R})} \nabla \times \mathbf{H}(\mathbf{r}) \right) \\ &= \nabla \times \left(\frac{1}{\epsilon(\mathbf{r})} \nabla \times \mathbf{H}(\mathbf{r}) \right) \\ &= \hat{\Theta} \mathbf{H}(\mathbf{r}). \end{aligned} \quad (1.19)$$

Since $[\hat{\mathbf{T}}_{\mathbf{R}}, \hat{\Theta}] = 0$, the operators $\hat{\mathbf{T}}_{\mathbf{R}}$ and $\hat{\Theta}$ have simultaneous eigenfunctions. Note that the set of plane waves $\exp[i(\mathbf{k} + l\mathbf{b}_1 + p\mathbf{b}_2) \cdot \mathbf{r}]$ are eigenfunctions of $\hat{\mathbf{T}}_{\mathbf{R}}$ with a degenerate eigenvalue of $\exp(-i\mathbf{k} \cdot \mathbf{R})$, it follows that the eigenfunction of $\hat{\Theta}$, which is also an eigenfunction of $\hat{\mathbf{T}}_{\mathbf{R}}$, can be expressed as a linear combination of the plane wave set specified by $\mathbf{k} = k_x \hat{\mathbf{x}} + k_y \hat{\mathbf{y}}$:

$$\begin{aligned} \mathbf{H}_{\mathbf{k}}(\mathbf{r}) &= \sum_{l,p} \mathbf{c}_{k_x,l} \exp \left[i \left(k_x + l \frac{2\pi}{a_1} \right) x \right] \mathbf{d}_{k_y,p} \exp \left[i \left(k_y + p \frac{2\pi}{a_2} \right) y \right] \\ &= \exp(ik_x x) \exp(ik_y y) \sum_{l,p} \mathbf{c}_{k_x,l} \exp \left(i \frac{2\pi l}{a} x \right) \mathbf{d}_{k_y,p} \exp \left(i \frac{2\pi p}{a} y \right) \\ &= \exp(i\mathbf{k} \cdot \mathbf{r}) \mathbf{u}_{\mathbf{k}}(\mathbf{r}) \end{aligned} \quad (1.20)$$

where $\mathbf{c}_{k_x,l}$ and $\mathbf{d}_{k_y,p}$ are expansion coefficients. It can be shown that $\mathbf{u}_{\mathbf{k}}$ is a periodic function that has the same periodicity as $\epsilon(\mathbf{r})$:

$$\begin{aligned}
\mathbf{u}_{\mathbf{k}}(\mathbf{r} + \mathbf{R}) &= \sum_{l,p} \mathbf{c}_{k_x,l} \exp\left(i\frac{2\pi l}{a}x + i2lm\pi\right) \mathbf{d}_{k_y,p} \exp\left(i\frac{2\pi p}{a}y + i2pn\pi\right) \\
&= \mathbf{u}_{\mathbf{k}}(\mathbf{r}).
\end{aligned} \tag{1.21}$$

This is known as the ‘‘Bloch theorem’’, which states that the eigenfunction of a periodic system is a ‘‘Bloch state’’ that can be written as a product of a plane wave and a periodic function. By examining Eq. 1.21, one can find that the Bloch state stays unchanged if the wave vector \mathbf{k} is replaced by $\mathbf{k}' = \mathbf{k} + l\mathbf{b}_1 + p\mathbf{b}_2$. It follows that the eigenvalue $(\omega/c)^2$ is identical for \mathbf{k} and \mathbf{k}' . Therefore, $\omega(\mathbf{k})$ is a periodic function in the k -space with periods given by the reciprocal vectors \mathbf{b}_1 and \mathbf{b}_2 . In the reciprocal lattice, the area determined by $|k_x| < \pi/a$ and $|k_y| < \pi/a$ is named the ‘‘first Brillouin zone’’. Although we only treated a simple square lattice here, it can be generalized to any 2-D and 3-D periodic structures in a similar manner as introduced here.

1.3 Superprism effect in a PC

Due to the banded structure of the dispersion relation in a PC, the direction of light’s group velocity can change rapidly with its frequency in certain regions near the photonic band edge. Compared to a conventional prism which changes the direction of light’s phase velocity upon refraction, this type of group velocity dispersion in PCs can happen within small propagation distance and result in a much larger angular change. This effect is named as ‘‘superprism effect’’ and studies have shown that it

is a promising candidate for constructing compact on-chip spectrometers or demultiplexers [45–48]. The mechanics behind the superprism effect can be illustrated with the aid of the equi-frequency contours (EFCs). The EFCs are the contours of the two dimensional dispersion relation function $\omega(k_x, k_y)$. In an isotropic medium, where the direction of propagation is of no importance, the dispersion relation reduces to $\omega(|\mathbf{k}|)$ which depends only on the magnitude of the wave vector. When the isotropy is broken, the EFCs prove to be a powerful tool to solve certain types of light propagation problems.

1.3.1 Refraction in terms of EFCs

Consider a case shown in Fig. 1.5(a) where a beam of light with a frequency ω_1 is incident on a dielectric medium with a refractive index n from vacuum. We choose the plane of incidence as the $x - y$ plane. In vacuum, the 2-D dispersion relation is

$$\omega_1(k_{x1}, k_{y1}) = c\sqrt{k_{x1}^2 + k_{y1}^2} \quad (1.22)$$

and that of the dielectric medium is

$$\omega_2(k_{x2}, k_{y2}) = c\sqrt{k_{x2}^2 + k_{y2}^2}/n \quad (1.23)$$

In the $k_x - k_y - \omega$ coordinates, these functions are plotted as two cones. The corresponding EFCs are two sets of concentric circles, as shown in Fig. 1.5(b). The magnitude and direction of the wave vector \mathbf{k}_2 can be determined from \mathbf{k}_1 using the EFCs as follows. When the light travels through the interface, the conservation of

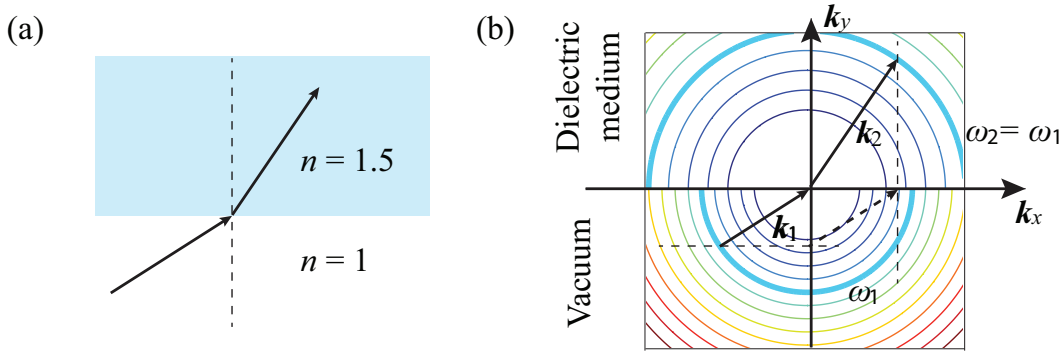


Figure 1.5: (a), Refraction of light at the interface between a dielectric medium and vacuum. The refractive index of the dielectric medium is $n = 1.5$. (b), an analysis of the refraction using EFCs. The EFCs of vacuum and the medium are plotted in the k space, separated by the k_x axis. \mathbf{k}_1 and \mathbf{k}_2 are the wave vectors in vacuum and the dielectric medium, respectively. To obtain \mathbf{k}_2 from \mathbf{k}_1 , note that the conservation of energy requires that $\omega_2 = \omega_1$. On the other hand, the boundary conditions state that $k_{x2} = k_{x1}$. It follows that a dashed line $k_x = k_{x1}$ intersects the EFC $\omega_2 = \omega_1$ at a point which is the end point of \mathbf{k}_2 .

energy requires that the frequency should not change, i.e. $\omega_2 = \omega_1$. Thus, the end point of the vector \mathbf{k}_2 must lie on the contour $\omega_2 = \omega_1$. Mathematically, combining equation 1.22 and 1.23, it follows that $\sqrt{k_{x2}^2 + k_{y2}^2} = n\sqrt{k_{x1}^2 + k_{y1}^2}$. The boundary conditions require a continuous k_x component along the interface. The direction of \mathbf{k}_2 can be determined by finding an appropriate point on the contour $\omega_2 = \omega_1$ which satisfies the condition $k_{x2} = k_{x1}$. It is simple to verify that the direction of the refracted light determined by this method agrees with the Snell's law.

1.3.2 Superprism in terms of EFCs

While the refraction problem described in last section can be easily solved by using the Snell's law, there is no alternative simple math formula when treating problems involving refraction at the surface of a PC. However, a band diagram of a PC can be calculated with numerical methods. Once the EFCs are known from the band diagram, the Bloch vectors of light inside the PC can be determined by taking into account the conservation of energy and the boundary condition as described in the previous section. In this section, EFCs in a PC are used to depict the superprism effect.

Assume two beams of light at the same frequency with wave vectors \mathbf{k}_1 and \mathbf{k}_2 along slightly different directions are propagating in a bulk medium before entering a PC region. Note that the definition of group velocity is $\mathbf{v}_g = \nabla_{\mathbf{k}}\omega(\mathbf{k})$. It follows that the direction of the group velocity is normal to the EFCs. In the bulk medium, the group velocities are collinear with the wave vectors since the EFCs are circles as shown in Fig. 1.6(c). Figure 1.6(d) shows the EFCs of the PC in the upper half of the first Brillouin zone calculated using plane wave expansion algorithm (MPB, [44]). The Bloch vectors \mathbf{k}'_1 and \mathbf{k}'_2 of the two beams inside the PC can be determined as described in the previous section. The angle between the two Bloch vectors is still small. However, the group velocities of the two beams are along two much differed directions. The superprism phenomenon arises from the drastic change in the group velocity along a non-circular EFC. Since the wave packet of a beam propagates along

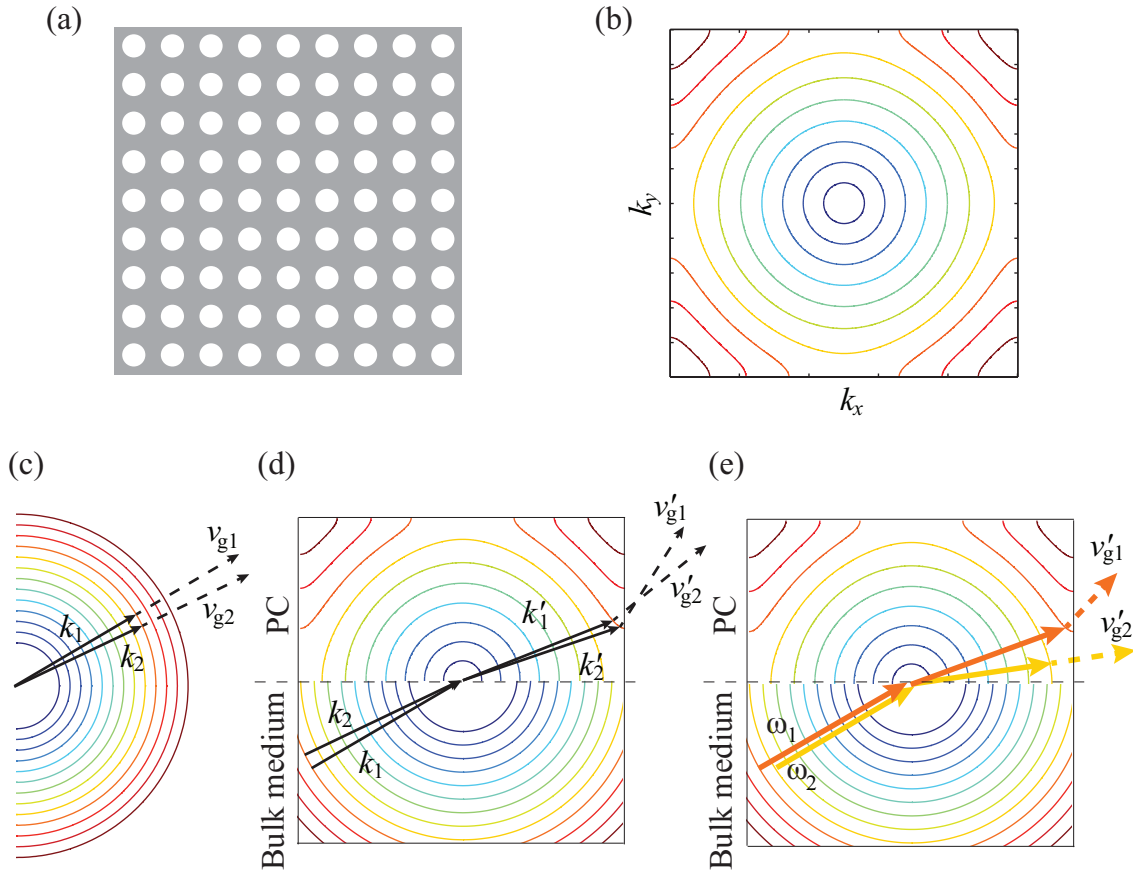


Figure 1.6: (a), Schematic diagram of a 2-D PC slab with a square lattice; (b), the EFCs of the PC in the first Brillouin zone; (c), the EFCs of an isotropic bulk medium. Two beams with wave vectors \mathbf{k}_1 and \mathbf{k}_2 propagate along the directions of their group velocities \mathbf{v}_1 and \mathbf{v}_2 , respectively. Since the EFCs are concentric circles, the group velocity of either beam is collinear with the wave vector of the beam. (d), superprism effect of beams with different incidence angles. Inside the PC region, the group velocity of a beam is no longer collinear with the Bloch wave vector. The directions of \mathbf{v}_1 and \mathbf{v}_2 differ by a larger amount than those of \mathbf{k}_1 and \mathbf{k}_2 do. (e), superprism effect of beams with different frequencies.

its group velocity, the two beams travel at very different directions and can be spatially separated after a short distance.

A similar analysis proves that instead of different angles of incidence, a small frequency change can also alter \mathbf{v}_g greatly due to the strong angular group velocity dispersion near the band edge, as shown in Fig. 1.6(e). Therefore, two beams with slightly different frequencies can be separated after propagating in the PC for a short distance. In this way, the superprism effect serves as a tool to resolve spectral components in a beam.

1.3.3 Negative diffraction in a PC

Aside from the superprism effect, the EFCs is also a convenient approach to illustrate the negative diffraction in a PC [49]. The phenomenon of normal diffraction can be analyzed using the angular-spectrum method. As shown in Fig. 1.7(a), a beam of finite size can be decomposed into a spectrum of plane waves using the Fourier transform at plane A. The spectrum contains a non-zero span of \mathbf{k} vectors near a center wave vector \mathbf{k}_0 . After a certain propagation distance, the beam profile at plane B can be calculated through an inverse Fourier transform while taking into account all the different phase shifts acquired by each of the plane wave components. In an isotropic bulk medium, a component with a wave vector \mathbf{k}_1 acquires a smaller amount of phase shift than the \mathbf{k}_0 component since the projection of \mathbf{k} onto the \mathbf{k}_0 direction is always smaller than \mathbf{k}_0 due to the concave shape of the circular EFCs, as

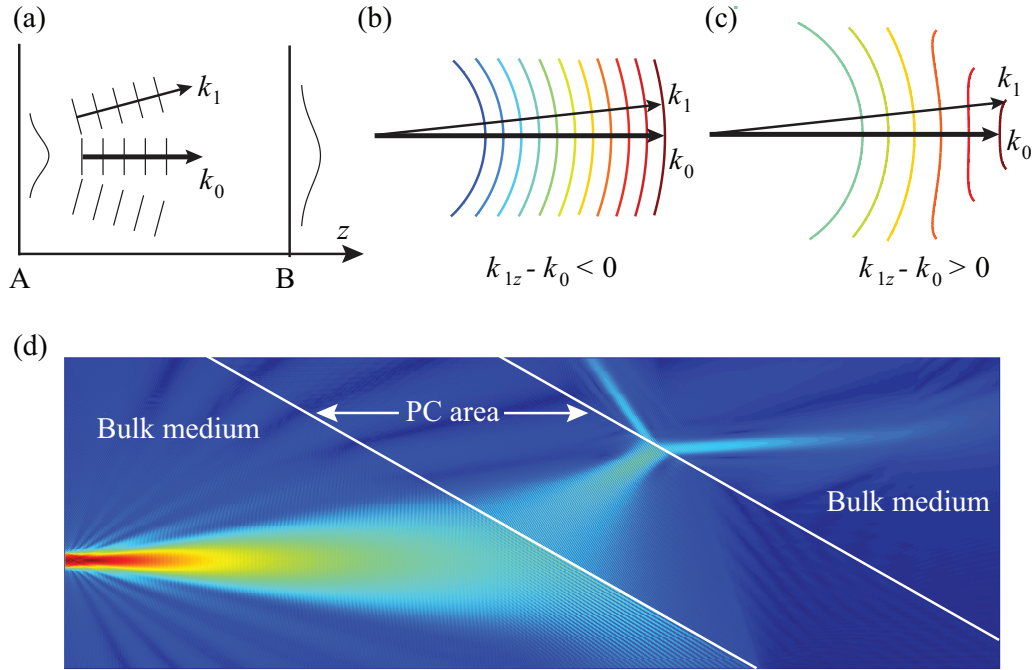


Figure 1.7: Negative diffraction. (a), a beam of finite size propagating along the z direction from plane A to plane B. Its angular spectrum contains a continuum of \mathbf{k} vectors centering on \mathbf{k}_0 . (b), the EFCs of an isotropic bulk medium. Since the EFCs are concave, $\mathbf{k}_{1z} - \mathbf{k}_0 < 0$ for $\mathbf{k}_1 \neq \mathbf{k}_0$. (c), EFCs of a PC. In the region where the contour is a convex curve, $\mathbf{k}_{1z} - \mathbf{k}_0 > 0$ for $\mathbf{k}_1 \neq \mathbf{k}_0$ is true. (d), the result of a FDTD simulation showing the effect of negative diffraction. A beam is preconditioned by free propagation in the bulk medium before it enters the PC area. Inside the PC area, the beam is focused again due to the negative diffraction.

shown in Fig. 1.7(b). The phase differences between different \mathbf{k}_1 components at plane B lead to the diffraction effect. In a PC, however, the opposite can happen at regions where the EFCs are convex curves as shown in Fig. 1.7(c). The phase difference between any \mathbf{k}_1 component and \mathbf{k}_0 plane wave has an opposite sign compared to that in the bulk medium. When a beam already preconditioned through free propagation in the bulk medium enters the PC, the phase differences between different plane waves will be reduced. The beam can be focused again after propagating in the PC as shown in Fig. 1.7(d). Because of the EFCs in the PC are not exact convex circular curves, this type of diffraction cancellation is not complete. Nonetheless, it offers a mechanism to reduce the beam sizes within the PC. When using the superprism effect to resolve spectral components in a beam, preconditioning is used to lower the cross talk between different channels [45, 46].

1.4 Defect-based PC nano-cavities and coupled-cavity waveguides (CCWs)

The superprism effect and the negative diffraction introduced in the previous section are two phenomena that can happen when light is traveling inside the PC. For light with frequencies in the photonic band gap, no propagation inside the PC is allowed. However, if the periodicity of an otherwise perfect PC is broken by a local defect, confined modes can exist at the defect in the photonic band gap. By purposely intro-

ducing a defect into the PC, a nano-cavity of the size comparable to the wavelength of light can be created [50]. A nano-cavity serves as an ultra-small filter under certain configurations [51, 52] since it is only “transparent” to light within the peak of the resonance in the frequency domain.

Among the many types of defect-based 2-D PC nano-cavities, the L-3 cavity is one of the most widely studied due to its high Q/v ratio [53], where “ v ” is the mode volume. An L-3 cavity is formed by removing three neighboring air holes in a hexagonal lattice PC as shown in Fig. 1.8(a). Figure 1.8(b) shows the electric field profile (E_y) of the fundamental resonant mode. Light is confined by Bragg reflections in the PC plane and by the total internal reflection (TIR) in the third direction. Consequently, the loss mechanism of an L-3 cavity can be categorized into in-plane loss and radiation loss. The in-plane loss is generally caused by material absorption and disorders in the PC including random fluctuations of air hole positions and irregular hole shapes due to fabrication imperfections. It can be reduced by choosing a proper host material and improving the fabrication procedure. Radiation loss, on the other hand, can be reduced by engineering the spatial profile of the resonant mode through tuning the positions and sizes of adjacent air holes [54]. To this date, a record Q factor of 2×10^6 has been reported in silicon nano-cavity [53].

When two or more identical nano-cavities are placed next to each other, light can couple from one cavity to another. As shown in Fig. 1.8(c), a series of L-3 cavities located along a straight line form a coupled-cavity waveguide (CCW) [55–57]. If the

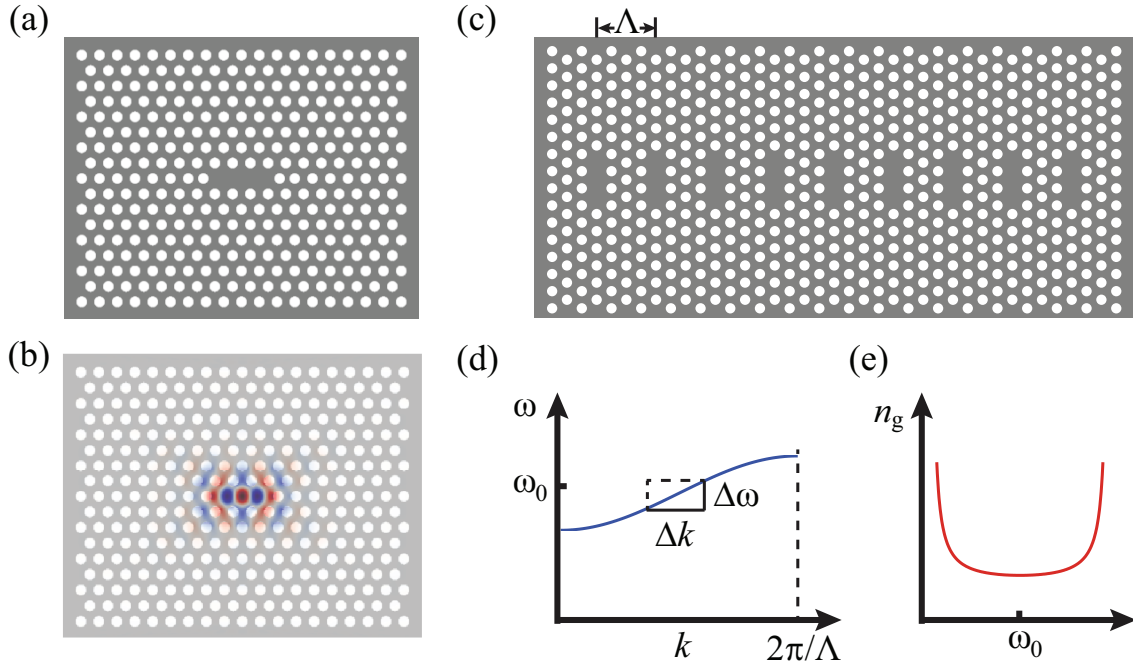


Figure 1.8: (a), An L-3 cavity. Three air holes are removed from a hexagonal lattice PC. (b), the electric field profile (E_y) of the fundamental resonant mode. The mode is confined by Bragg reflection in all directions in the PC plane. (c), a coupled-cavity waveguide (CCW) composed of a series of L-3 cavities. The distance between neighboring cavities is $\Lambda = 2\sqrt{3}a$ where “ a ” is the lattice constant of the PC. (d), dispersion profile predicted by the tight-binding approximation. Only effects from the nearest neighbors are considered. (e), group index as a function of frequency. Near the center frequency ω_0 , the curve shows a uniform behavior.

cavities are weakly coupled, the dispersion profile of the CCW can be qualitatively described by the tight-binding approximation model developed in solid state physics [55]. Specifically, the following two arguments are taken into account when seeking the dispersion relation of the CCW: 1, for a periodic dielectric structure, the solution to the Maxwell equations should also be periodic with the same period according to the Bloch theorem; 2, since the coupling is weak, the electric field profile around each cavity of the CCW is essentially the same as that of an isolated cavity. Under these conditions, assuming the cavities are separated by a distance Λ in the x -direction, the eigenmode of the CCW can be written as a linear combination of the eigenmodes of isolated cavities:

$$\begin{aligned}\mathbf{E}_{CCW}(\mathbf{r}, t) &= \exp(i\omega_k t)\mathbf{E}_{CCW}(\mathbf{r}) \\ &= C \exp(i\omega_k t) \sum_n \exp(-ink\Lambda)\mathbf{E}_0(\mathbf{r} - n\Lambda\mathbf{e}_x)\end{aligned}\tag{1.24}$$

where C is a normalization constant to ensure that $\int |\mathbf{E}_{CCW}(\mathbf{r})|^2 d^3\mathbf{r} = 1$ and $\mathbf{E}_0(\mathbf{r})$ is the normalized eigenmode of an isolated cavity located at the origin. Since both $\mathbf{E}_{CCW}(\mathbf{r})$ and $\mathbf{E}_0(\mathbf{r})$ are solutions of the Maxwell equations, they satisfy the following relations:

$$\nabla \times \nabla \times \mathbf{E}_{CCW}(\mathbf{r}) = \epsilon(\mathbf{r}) \frac{\omega_k^2}{c^2} \mathbf{E}_{CCW}(\mathbf{r}),\tag{1.25}$$

$$\nabla \times \nabla \times \mathbf{E}_0(\mathbf{r}) = \epsilon_0(\mathbf{r}) \frac{\omega_0^2}{c^2} \mathbf{E}_0(\mathbf{r}),\tag{1.26}$$

where $\epsilon(\mathbf{r})$ is the dielectric constant profile of the CCW, $\epsilon_0(\mathbf{r})$ that of an isolated cavity sitting at the origin, and ω_0 the resonant frequency of an isolated cavity. To get the dispersion relation $\omega_k(k)$, one can apply $\mathbf{E}_0^*(\mathbf{r})$ on both sides of equation

1.25 and take the inner product by integrating over the entire space, then substitute equations 1.24 and 1.26 into it, the eigenvalue ω_k can be expressed as:

$$\omega_k^2 = \omega_0^2 \frac{1 + \sum_{n \neq 0} \exp(-ink\Lambda) \beta_n}{1 + \Delta\alpha + \sum_{n \neq 0} \exp(-ink\Lambda) \alpha_n}, \quad (1.27)$$

where α_n , β_n and $\Delta\alpha$ are defined as:

$$\begin{aligned} \alpha_n &= \int d^3\mathbf{r} \epsilon(\mathbf{r}) \mathbf{E}_0^*(\mathbf{r}) \mathbf{E}_0(\mathbf{r} - n\Lambda \mathbf{e}_x), \quad n \neq 0, \\ \beta_n &= \int d^3\mathbf{r} \epsilon_0(\mathbf{r} - n\Lambda \mathbf{e}_x) \mathbf{E}_0^*(\mathbf{r}) \mathbf{E}_0(\mathbf{r} - n\Lambda \mathbf{e}_x), \quad n \neq 0, \\ \Delta\alpha &= \int d^3\mathbf{r} [\epsilon(\mathbf{r}) - \epsilon_0(\mathbf{r})] \mathbf{E}_0^*(\mathbf{r}) \mathbf{E}_0(\mathbf{r}). \end{aligned} \quad (1.28)$$

Similar to the discussion in section 1.2.3, the choice of the Bloch wavevector k is limited to the first Brillouin zone $|k| \leq \pi/\Lambda$. For weakly coupled high- Q cavities, the resonant field profile of each cavity is tightly confined within the cavity area and the overlapping of fields between neighboring cavities is small. Consequently, we can set $\alpha_n = 0$, $\beta_n = 0$ for all $|n| > 1$ and only keep the small interaction terms $\alpha_{\pm 1}$, $\beta_{\pm 1}$. The symmetry of the structure further indicates that $\alpha_1 = \alpha_{-1}$ and $\beta_1 = \beta_{-1}$. The dispersion relation can be calculated from equation 1.27 as:

$$\begin{aligned} \omega &= \omega_0 [1 + 2\beta_1 \cos(k\Lambda)]^{\frac{1}{2}} [1 + \Delta\alpha + 2\alpha_1 \cos(k\Lambda)]^{-\frac{1}{2}} \\ &\approx \omega_0 [1 + \beta_1 \cos(k\Lambda)] [1 - \Delta\alpha/2 - \alpha_1 \cos(k\Lambda)] \\ &\approx \omega_0 [1 - \Delta\alpha/2 - \kappa \cos(k\Lambda)], \end{aligned} \quad (1.29)$$

where $\kappa = \alpha_1 - \beta_1$. In addition, $\Delta\alpha$ is a higher-order small quantity compared to $\alpha_{\pm 1}$ and $\beta_{\pm 1}$ since $\epsilon(\mathbf{r}) - \epsilon_0(\mathbf{r})$ is non-zero only at areas that are located at least Λ away

from the origin, where $\mathbf{E}_0(\mathbf{r})$ is small and $|\mathbf{E}_0(\mathbf{r})|^2$ is a higher-order small quantity.

When $\Delta\alpha$ is negligible, equation 1.29 turns into:

$$\omega_k \approx \omega_0[1 - \kappa \cos(k\Lambda)]. \quad (1.30)$$

Near the center frequency ω_0 , the dispersion curve is approximately linear as shown in Fig. 1.8(d). Note that the group velocity is defined as

$$v_g = d\omega/dk \approx \Delta\omega/\Delta k. \quad (1.31)$$

It follows that by reducing $\Delta\omega$ and increasing Δk , slow-light can be realized in a CCW. In addition, the approximately linear dispersion curve also leads to a uniform group index profile near the center frequency ω_0 , as shown in Fig. 1.8(e). In chapter 5, we will investigate the application of CCWs in slow-light spectroscopy [58–61].

2 The design of a flat-band PC superprism

As described in section 1.3, when beams with slightly different frequencies enter a PC, the superprism effect can take place and result in a large angular separation. The two beams will separate over a short propagation distance in a 2-D PC slab. This compactness is ideal for on-chip miniature spectrometer designs. Many previous studies of the superprism effect concentrated only on achieving an angular dispersion as large as possible. However, large angular dispersion typically occurs only over a very narrow range of frequencies near the photonic band-edge, and is highly frequency dependent. Using such a superprism structure to construct a spectrometer would lead to highly nonuniform channel spacing over a narrow working bandwidth.

On the contrary, an ideal spectrometer would possess uniform spectral resolution over a large working bandwidth, i.e., would possess a flat-top dispersion profile. To incorporate such an idea into the design of a superprism structure, we here propose a new figure of merit (FOM), namely the angular-group-dispersion–bandwidth product

(AGDBP) to quantitatively describe the spectroscopic performance of PC superprism structures. Using this new metric, we perform an optimization of the geometry of a two-dimensional parallelogram-lattice PC structure to achieve flat-band operation. The spectral performance of one example of a superprism-based on-chip spectrometer is further analyzed numerically using finite-difference time-domain (FDTD) simulations.

2.1 A quantitative analysis of the superprism effect

Section 1.3 provides a powerful tool to understand the superprism effect: the EFCs. In addition, EFCs also offer a way to numerically study the strength of the superprism effect, once the band structure of a lattice is known. In this section, we first briefly summarize the mathematical formula used to quantitatively describe the angular dispersion performance of a given superprism PC structure with the aid of EFCs.

We start with a 2-D square-lattice PC structure as shown in the inset of Fig. 2.1, where “ \mathbf{a}_1 ” and “ \mathbf{a}_2 ” are the primitive lattice vectors and r is the radius of each air hole. We use a plane wave expansion analysis algorithm [44] to calculate the bandstructure of such a PC. The host material is assigned to be a silicon-on-insulator (SOI) wafer with a typical effective index $n = 2.83$ in 2-D simulations for TE modes near 1550 nm [62, 63]. The calculated EFC for the TE modes in the first Brillouin

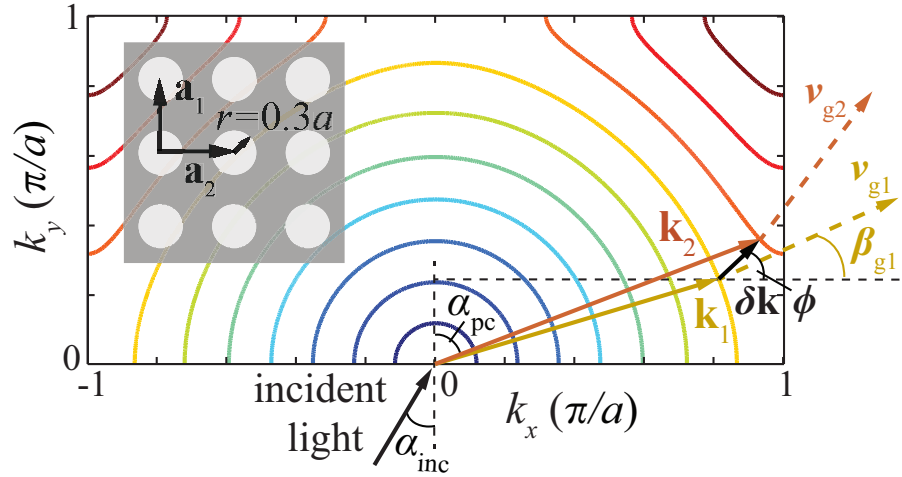


Figure 2.1: Equi-frequency contours (EFCs) of a 2-D square lattice PC in the first Brillouin zone. The light beam enters the PC region at an incidence angle α_{inc} and the “refraction” angle inside the PC region is labeled as α_{pc} . Solid arrows are the Bloch \mathbf{k} vectors which also represent the direction of phase velocities of the beams. Dashed arrows are normal to the EFC contour, indicating the directions of group velocities. Strong anisotropy leads to deviations of the EFCs from perfect circles. Near the band edge in k -space, a small change in frequency leads to a large directional variation in group velocity. Inset: the PC structure in real space. \mathbf{a}_1 and \mathbf{a}_2 are the two primitive lattice vectors. The radius of the air holes is $r = 0.3a$ where $a = |\mathbf{a}_1|$ is the lattice constant.

zone are plotted in Fig. 2.1.

Assume that the interface between the PC and the incident slab medium is along one lattice direction, denoted by \mathbf{a}_1 . To quantify the superprism effect, define the angular group dispersion (AGD), also sometimes referred to as the q factor [64] at a frequency ω as follows:

$$q(\alpha_{\text{inc}}, \omega) = \left. \frac{\partial \beta_g}{\partial \omega} \right|_{\alpha_{\text{inc}}}, \quad (2.1)$$

where “ α_{inc} ” is the incidence angle from a slab medium with an effective refractive index n_{slab} , and “ β_g ” denotes the angle between the group velocity vector and the k_x -axis. By definition, $\mathbf{v}_g = \nabla_{\mathbf{k}}\omega(\mathbf{k})$, the value of β_g can be obtained using the following equation:

$$\tan \beta_g = \frac{v_{gy}}{v_{gx}} = \frac{\partial \omega / \partial k_y}{\partial \omega / \partial k_x}. \quad (2.2)$$

Since one can obtain the numerical values of the partial derivatives $\partial \omega / \partial k_x$ and $\partial \omega / \partial k_y$ by analyzing the calculated band structure, expression (2.1) can be rewritten as follows:

$$q = \frac{\partial \beta_g / \partial \mathbf{k} |_{\alpha_{\text{inc}}}}{\partial \omega / \partial \mathbf{k} |_{\alpha_{\text{inc}}}}. \quad (2.3)$$

For light incident from a fixed direction, a frequency change $\delta \omega$ leads to a change in the Bloch wave vector \mathbf{k} inside the PC as follows:

$$\delta \mathbf{k} = \frac{\delta \omega}{d\omega/dk_\phi} \hat{\mathbf{u}}_\phi, \quad (2.4)$$

where “ $\hat{\mathbf{u}}_\phi$ ” is the unit vector along $\delta \mathbf{k}$ and “ ϕ ” is the angle between this vector and the k_x axis. Employing the boundary conditions at the interface and solving for ϕ ,

we have

$$\tan \phi = \left(\frac{\omega}{|k| \sin \alpha_{\text{phc}}} - \frac{\partial \omega}{\partial k_x} \right) / \frac{\partial \omega}{\partial k_y}, \quad (2.5)$$

where “ α_{phc} ” is the effective refraction angle of the incident field within the PC region.

This relation determines the direction of the derivatives in Eq. (2) that should be taken, and the numerical values of q can eventually be determined using numerically obtainable quantities as follows:

$$q = \frac{\left(\frac{\partial \omega}{\partial k_x} \frac{\partial^2 \omega}{\partial k_x \partial k_y} - \frac{\partial^2 \omega}{\partial k_x^2} \frac{\partial \omega}{\partial k_y} \right) \cos \phi + \left(\frac{\partial \omega}{\partial k_x} \frac{\partial^2 \omega}{\partial k_y^2} - \frac{\partial^2 \omega}{\partial k_x \partial k_y} \frac{\partial \omega}{\partial k_y} \right) \sin \phi}{\left[\frac{\partial \omega}{\partial k_x} \cos \phi + \frac{\partial \omega}{\partial k_y} \sin \phi \right] \left[\left(\frac{\partial \omega}{\partial k_x} \right)^2 + \left(\frac{\partial \omega}{\partial k_y} \right)^2 \right]}. \quad (2.6)$$

2.2 Lattice Structure Optimization

One major limitation of a square-lattice PC superprism structure is that its AGD is highly frequency dependent, which leads to very narrow working bandwidth over which the superprism effect is appreciable and to very unevenly-spaced channel spacing.

For spectroscopic applications, one typically is concerned about how many uniformly-distributed spectral lines a spectrometer can resolve over the bandwidth of interest. Such concern indicates that an ideal superprism spectrometer should have uniform AGD over an extended working bandwidth. To take into account such considerations, we here propose a new figure of merit, namely the angular-group-dispersion-

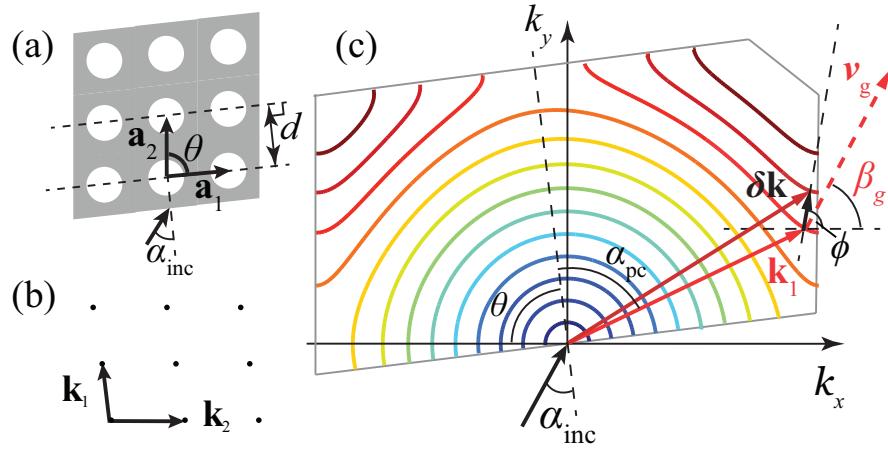


Figure 2.2: Geometric analysis of beam propagation in a general 2-D PC. (a), the PC structure in coordinate space; θ and d are the two adjustable parameters; (b), corresponding reciprocal lattice; \mathbf{k}_1 is perpendicular to \mathbf{a}_1 and \mathbf{k}_2 to \mathbf{a}_2 . (c), EFC plot of the structure. The k_x axis is chosen to be along the \mathbf{k}_2 direction.

bandwidth product (AGDBP) defined as follows:

$$\mathcal{P}(\omega_0) = q(\omega_0)\Delta\omega. \quad (2.7)$$

Here $q(\omega_0)$ is the AGD at a central frequency ω_0 , and $\Delta\omega$ is the frequency bandwidth in the vicinity of ω_0 within which the AGD varies less than 5% from $q(\omega_0)$. To optimize the PC structure to achieve a flat-band spectral performance, we generalize the square PC lattice into a parallelogram lattice as shown in Fig. 2.2(a) and (b). A parallelogram lattice can be described using several free parameters: the angle θ between the two primitive lattice vectors \mathbf{a}_1 and \mathbf{a}_2 , and the distance d between neighboring rows of air holes, and the radius of air holes r . For illustrative purposes, we here choose to fix r at a typical value $r = 0.3a$ and to optimize only the two

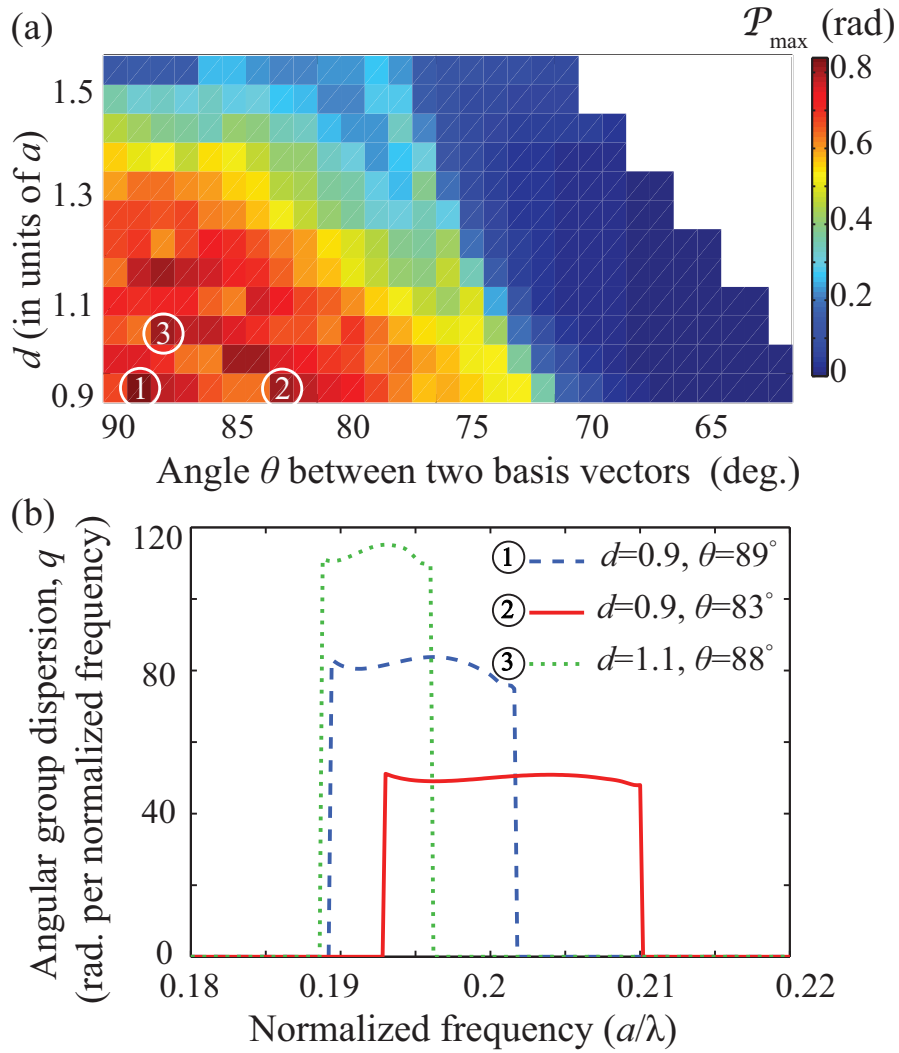


Figure 2.3: Optimization results for obtaining a flat-band PC superprism. (a), Maximum value of the angular-group-dispersion bandwidth product (AGDBP) \mathcal{P}_{\max} as a function of position in the two dimensional parameter space; (b), Superprism factor q as a function of the normalized frequency ω plotted for 3 structures: ① $\mathcal{P}_{\max} = 0.839$ rad, $d = 0.9a_1, \theta = 89^\circ$; ② $\mathcal{P}_{\max} = 0.802$ rad, $d = 0.9a_1, \theta = 83^\circ$; ③ $\mathcal{P}_{\max} = 0.809$ rad, $d = 1.1a_1, \theta = 88^\circ$.

parameters θ and d . Note that $|\mathbf{a}_2| \equiv a_2 = d/\cos\theta$.

For a given PC structure with a set of values for θ and d , we first calculate the value of \mathcal{P} for all possible incidence angle α_{inc} as shown in Fig. 2.2(a) using the procedure described in the previous section. We then select the maximum value \mathcal{P}_{max} as the optimum AGDBP of the structure with the current set of θ and d . Considering practical fabrication conditions, we here limit the value of d to be between $0.9a_1$ and $1.5a_1$, and the value of θ between 90° and $90^\circ - \tan^{-1}(0.5a_1/d)$. Note that for a given value of d , our scanning range of θ covers all possible geometries for all incidence angles due to the symmetry and periodicity of the PC structures.

The optimum AGDBP \mathcal{P}_{max} is plotted in Fig. 2.3(a) as a function of θ and d . Figure 2.3(b) shows the optimized AGD as a function of frequency for three different sets of optimized parameters as circled in Fig. 2.3(a). All three of these designs exhibit flat-band AGD over different frequency ranges, and therefore can satisfy various differing needs for the working bandwidth.

2.3 Finite difference time domain (FDTD) simulation of a flat-band superprism

The spectral performance of an optimized superprism spectrometer is simulated using finite-difference time-domain (FDTD) algorithms [65]. The lattice parameter of the PC structure is chosen to be $d = 0.9a_1, \theta = 89^\circ$, i.e., the structure ① marked in

Fig. 2.3(b). The lattice constant is a_1 to be 310 nm, which would set the center wavelength at 1550 nm with a working bandwidth of approximately 80 nm.

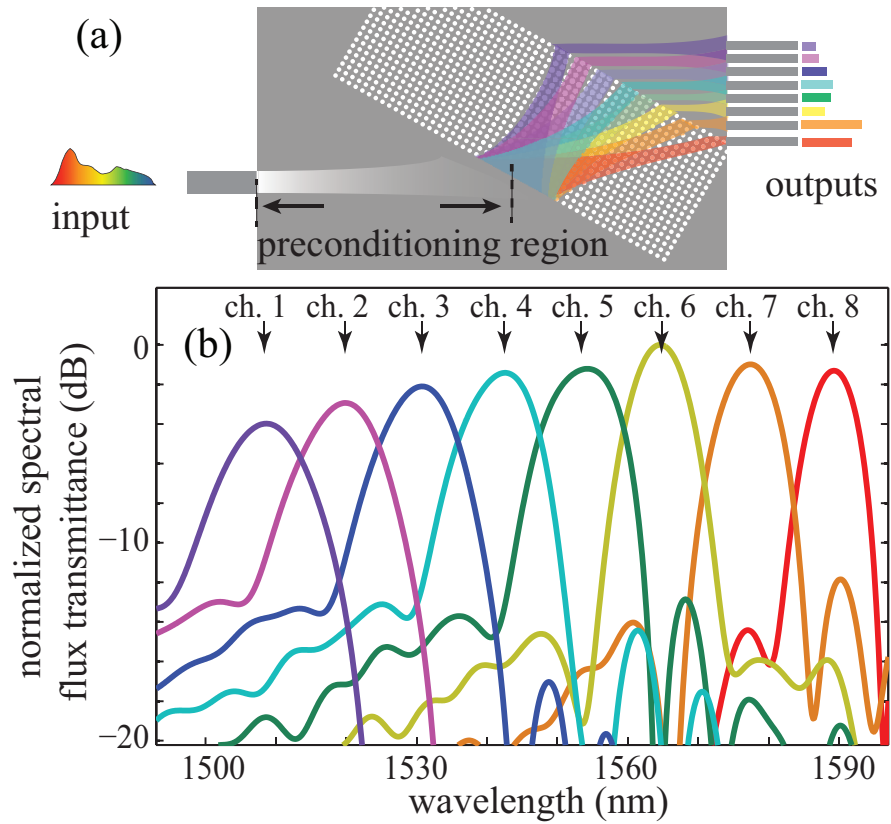


Figure 2.4: (a) Schematic diagram of a flat-band superprism spectrometer; (b) spectral transmission of the 8 channels that are evenly spaced over the working bandwidth.

The schematic diagram of this spectrometer is shown in Fig. 2.4(a). The device is composed of an adiabatically tapered input waveguide, a preconditioning free-propagation region (a slab waveguide) [46], a PC superprism region, a second free-propagation slab region, and a series of single-mode output waveguides corresponding

to individual output channels. Light is launched into the structure from the input waveguide. This input waveguide is adiabatically widened to an exit-width of $3.72 \mu\text{m}$ in order to reduce the angular spatial frequency components of the input beam. The preconditioning region is designed to be $140 \mu\text{m}$ long and has opposite sign in the second-order diffraction coefficient [49] as compared to that in the PC region. As a result, the beam first diverges in the preconditioning region and then re-focuses as it propagates within the PC region. The spacing between neighboring output waveguides is approximately $3.5 \mu\text{m}$. The output signals are coupled into 8 single-mode waveguides. Figure 2.4(b) shows the normalized spectral transmittance of the 8 channels. As predicted by the design, this device shows a very flat spectral response over its designed working bandwidth, and the number of channels it can support is approximately doubled as compared to previous designs [45–48]. The total PC area is approximately $135 \text{ by } 42 \mu\text{m}^2$. The crosstalk of the device is primarily caused by the aberration of the system and can be further reduced by optimizing the shape and local lattice geometries of the PC region [66].

3 Experimental study of a flat-band silicon superprism

In the previous chapter, we developed a method to systematically optimize a superprism for a flat-band operation. Guided by the optimization results, we fabricated several real devices on a piece of SOI wafer. In this chapter, the spectral performances of these devices are characterized and discussed.

3.1 AGD in a PC superprism

The 2-D effective index of the host material introduced in section 2.1 was chosen based on the specifications of typical SOI wafers with a 220-nm-thick silicon layer deposited on a 1- μm -thick silica layer. Since light in the silicon layer is confined by TIR in the vertical direction, we improve the vertical index-guiding by removing the silica substrate through under etching and achieve a symmetric index profile across the silicon membrane. We performed the bandstructure calculation and lattice optimization

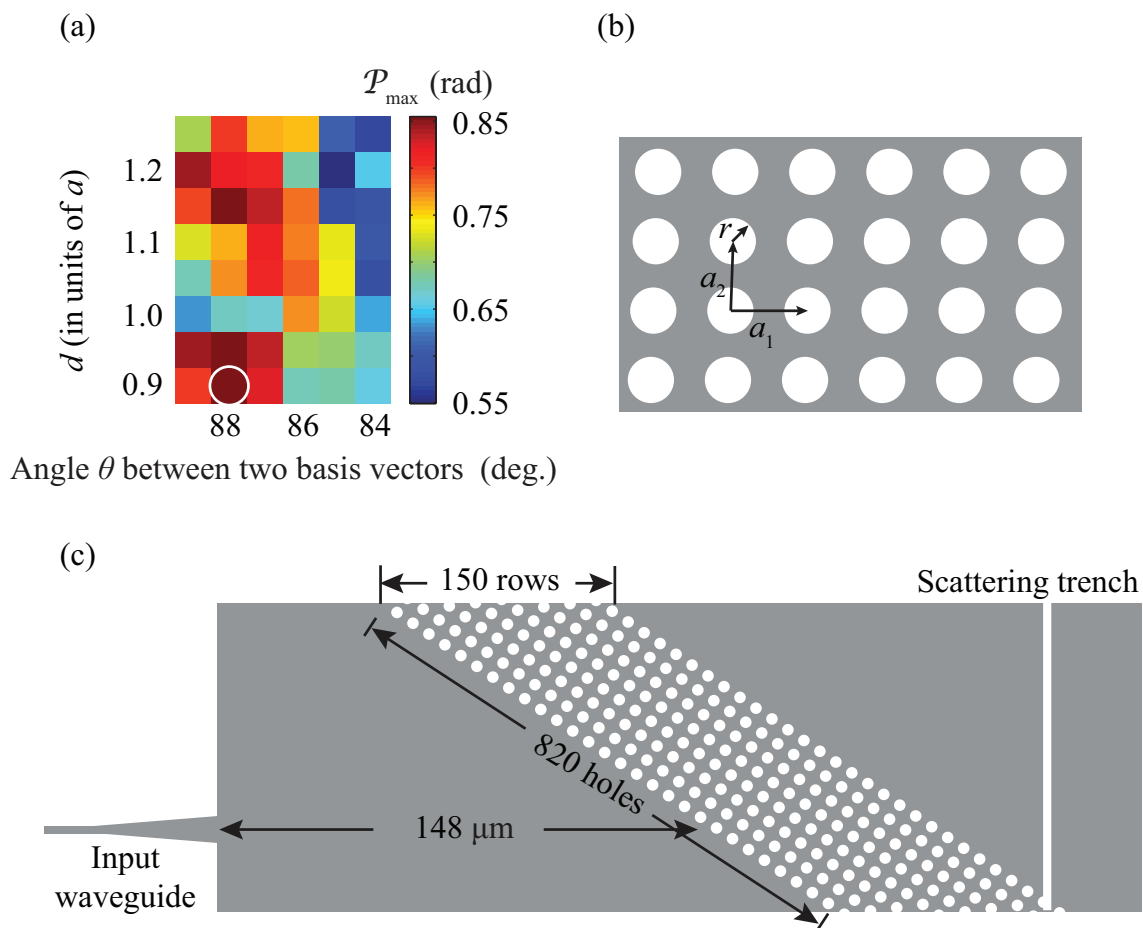


Figure 3.1: (a), Maximum value of the AGDBP \mathcal{P}_{\max} as a function of position in the two dimensional parameter space; (b), the lattice of the PC; (c), schematic diagram of the superprism structure.

introduced in section 2.2 concerning this difference. The optimum AGDBP (\mathcal{P}_{\max}) is found to be 0.8548 rad when $d = 0.9a_1$ and $\theta = 88^\circ$. The geometry of the PC is shown in Fig. 3.1(b) where the two lattice constants are $a_1 = 330$ nm and $a_2 = 297.181$ nm. Figure 3.1(c) shows the schematics of the entire structure including an input waveguide, a precondition area, the PC area and a scattering trench to vertically scatter light out of the PC plane. The PC area is composed of 820×150 air holes. The position of the trench is chosen to be where the average beam size of transmitted light within the working bandwidth is minimized according to simulations. We then fabricated the designed structure using e-beam lithography.

We employed an end-fire coupling system shown in Fig. 3.2(a) to characterize the fabricated sample. Light from a Santec TSL-510 tunable laser is coupled into a piece of tapered SMF-28 fiber with a $2.5 \mu\text{m}$ spot diameter and a $14 \mu\text{m}$ working distance. A manual fiber polarization controller is used to maximize the coupling efficiency into the input waveguide which supports the TE mode. After propagating through the precondition area and the PC area, light is scattered out of the plane by the trench and collected by a Xenics Xeva-1.7-640 infrared camera after a 20x microscope objective. Figure 3.2(b) shows the scattering trench and the PC area under infrared illumination. We define the x -axis to be along the trench and point toward the PC area. The laser wavelength is tuned from 1500 nm to 1630 nm with a 1 nm step size. At each step, the camera takes one image to record the x -coordinate and intensity of the scattered light as shown in Fig. 3.2(c). The small size of the spot

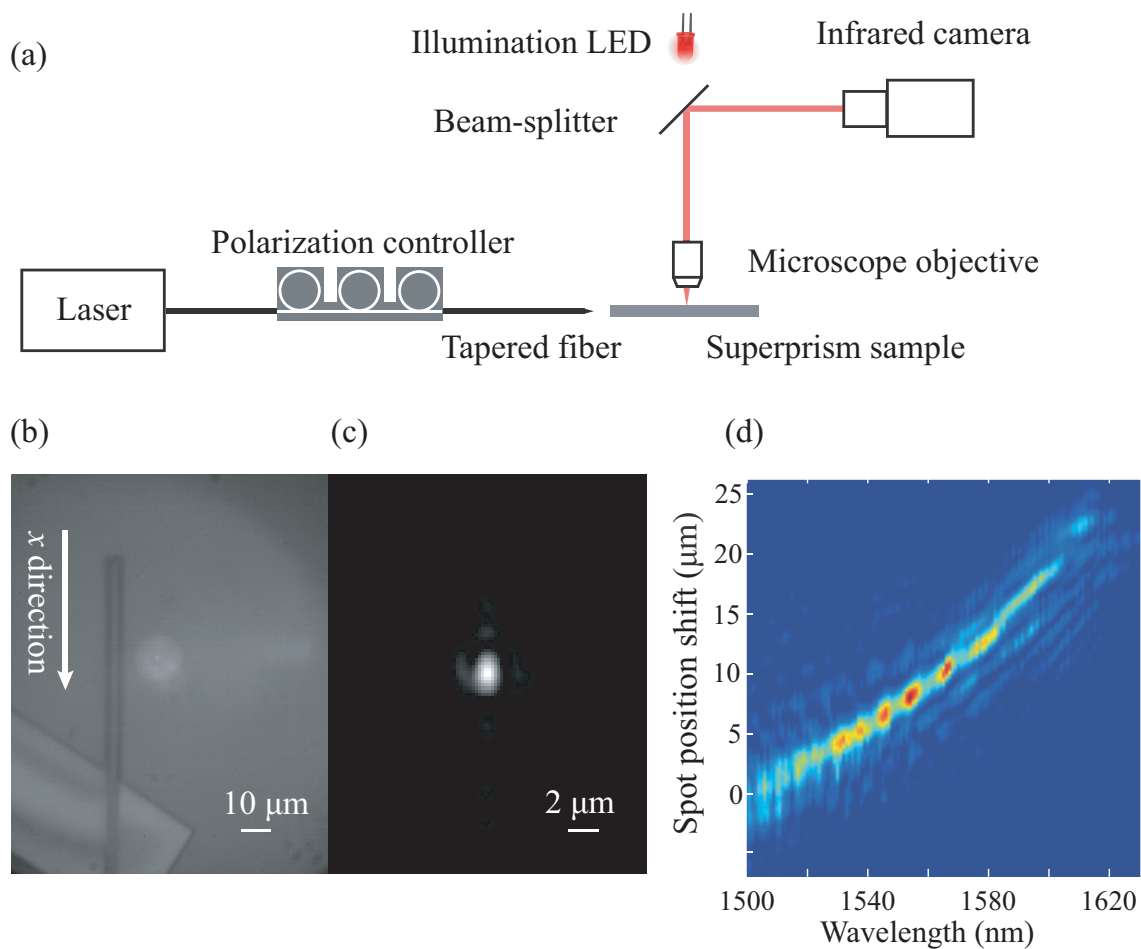


Figure 3.2: (a), End-fire coupling system; (b), an image of the scattering trench and part of the PC region under infrared illumination. The x direction is defined as shown. Scale bar is displayed at the bottom right corner. (c), light scattered from the trench; (d), spot position along the x axis versus input wavelength.

confirms that the preconditioned light experienced a negative diffraction in the PC area. Figure 3.2(d) shows the results over a 131 nm wavelength span. The maximum position shift in x direction is measured to be $21.5 \mu\text{m}$ between light with 1500 nm and 1600 nm wavelengths. Considering the geometry parameters of the PC area, the corresponding angle between the two group velocities is estimated to be 0.82 rad, while our simulated \mathcal{P}_{max} has a value of 0.8548 rad. The experimental results show a good agreement to our design of a flat-band superprism.

3.2 An 8 channel on-chip superprism spectrometer

Encouraged by the findings in the previous section, we replaced the scattering trench in the design with 8 single mode out-put waveguides to build an 8-channel on-chip superprism spectrometer as shown in Fig. 3.3(a). The waveguides are labeled as “WG1” to “WG8” and their positions are determined by FDTD simulations to achieve a channel spacing of 12 nm. Figure 3.3(b) shows an image of the waveguides under infrared illumination. Light scattered at the end of the waveguides is collected by the infrared camera. The frequency responses of all 8 waveguides are plotted in Fig. 3.3(c). Because of that WG1 and WG8 are located at the edge of the working bandwidth, they suffer from a higher crosstalk. This can be improved by modifying the precondition distance and the angle of incidence in the design following results from simulations with much higher resolutions in the algorithms. Alternatively, from an application point of view, the current device can function as a 6 channel on-chip

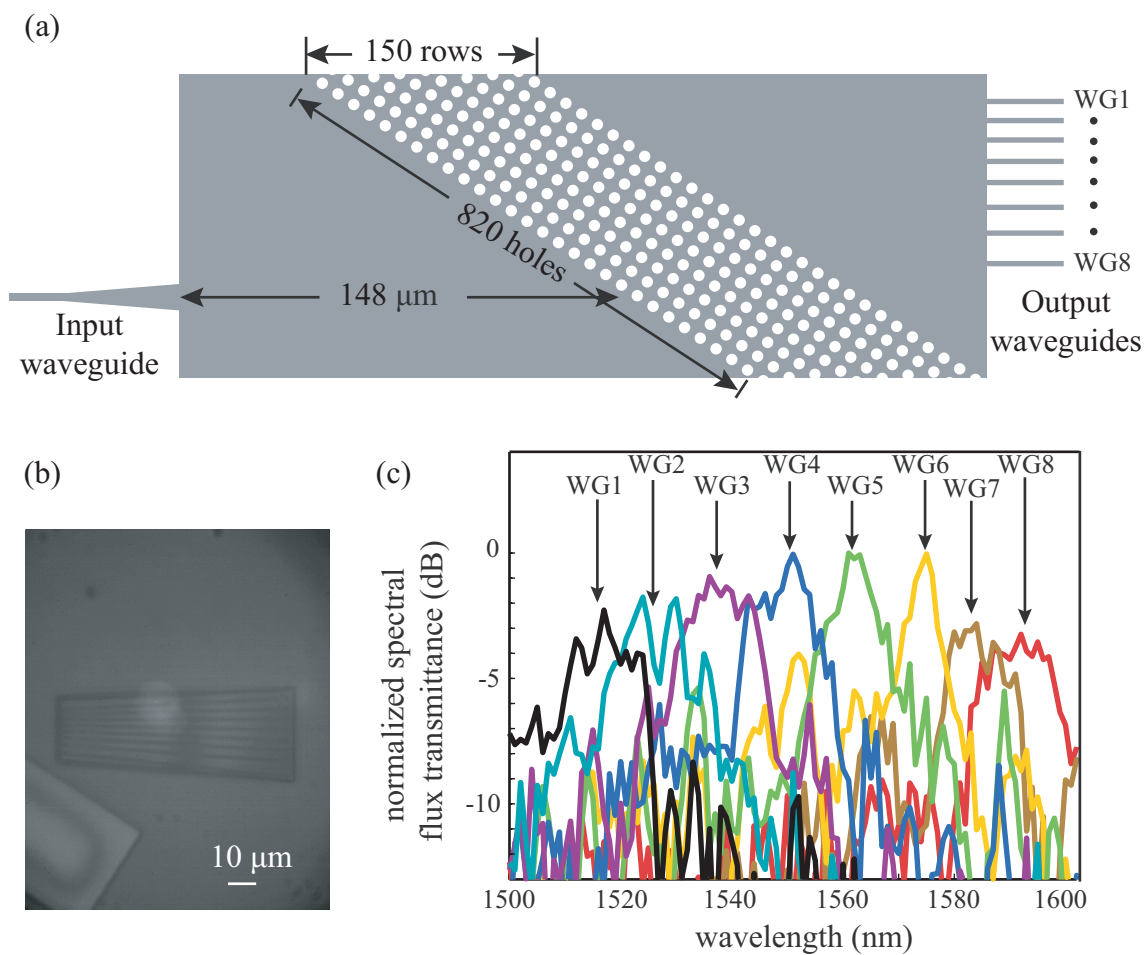


Figure 3.3: (a), Schematic diagram of an 8 channel superprism spectrometer; (b), image of eight single-mode output waveguides; (c), the spectral flux transmission measured at the end of eight output waveguides.

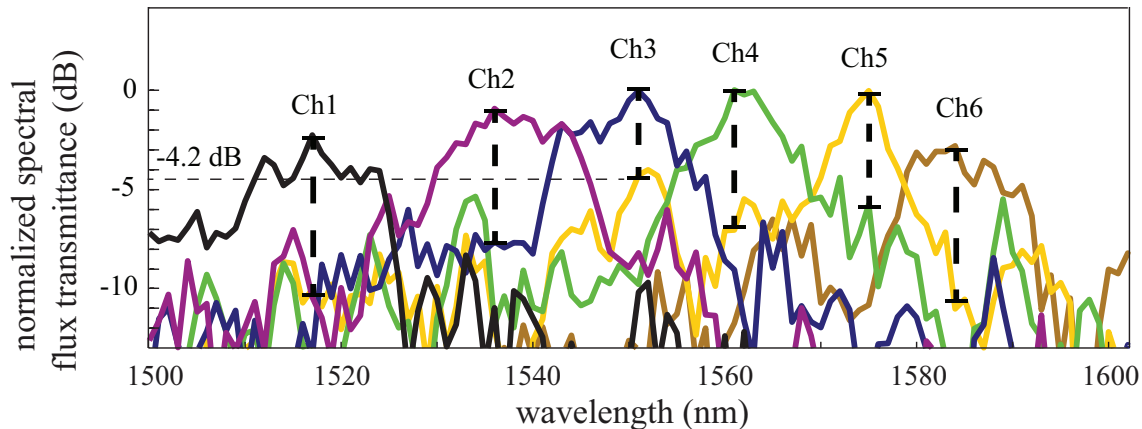


Figure 3.4: Spectral flux transmission from 6 channels. The maximum inter-channel crosstalk is -4.2 dB induced by channel 3 in channel 5.

spectrometer if the signals from WG2 and WG8 were ignored, as shown in Fig. 3.4. The inter-channel crosstalk is estimated to be less than -4.2 dB. The working spectral range is estimated to be from 1510 nm to 1600 nm. Compared to previously reported 4-channel superprism spectrometers [46, 48], the total number of working channels is 50% higher. To better evaluate the advantages and disadvantages of our design, we also compare our device with several other types of on-chip compact spectrometers published in literatures. Several FOMs of interest are listed in table 3.1: the spectral range, the spectral resolution, the number of resolvable channels N and the footprint of the device S . The ratio N/\sqrt{S} is also listed and serves as one way to describe the “spatial efficiency” of various designs. Note that for different applications, some of the FOMs can be much more desirable than others. Therefore, one should choose the appropriate design regarding the specific goals and requirements.

Design	Spectral range	$\delta\lambda$	N	Footprint, S	N/\sqrt{S} (mm^{-1})
Arrayed-waveguide grating [67]	1530~1565 nm	68 pm	512	11 mm×16 mm	38.6
Cascaded M-Z interferometers [68]	1549.625~ 1550.375 nm	42 pm	18	12 mm^2	5.2
Flat-band superprism (this work)	1510~1600 nm	15 nm	6	220 $\mu\text{m} \times 120 \mu\text{m}$	37
Nanocavities array* [69]	805~840 nm	0.35 nm	100	50 $\mu\text{m} \times 50 \mu\text{m}$	2000
Disordered photonic chip** [70]	1500~1525 nm	0.75	33	25 $\mu\text{m} \times 50 \mu\text{m}$	933

Table 3.1: Comparison between several types of on-chip compact spectrometers.

$\delta\lambda$: spectral resolution. N : number of resolvable channels. *: the nanocavities array requires additional vertical out-coupling setup for far-field emission detection. **: the disordered photonic chip design relies on computational methods to extract the spectral information from measured signals, thus additional computer hardware and software are necessary.

4 On-chip spectroscopy with thermally tuned high- Q PC cavities

The superprism structures studied in the last two chapters employ the AGD as a wavelength resolving mechanism. Compared to a traditional prism, it has a very small foot print. Nonetheless, similar to all other types of dispersive spectrometers, it has a resolution in wavenumbers (cm^{-1}) typically given by $1/L$, where L is the characteristic size of the dispersive region in cm. To overcome this limitation, we investigate miniature spectrometer designs based on PC nano-cavities introduced in section 1.4.

One design proposed by Gan *et al.* [69] is shown schematically in Fig. 4.1(a). The spectrometer is composed of a bus waveguide coupled to a series of PC nano-cavities with different resonant wavelengths. Light scattered vertically by each nano-cavity is collected and measured to reconstruct the input spectrum injected in the

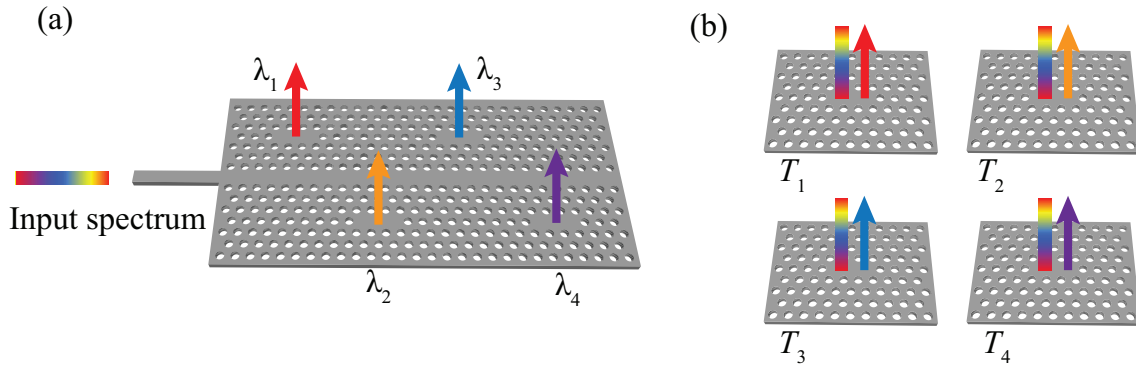


Figure 4.1: Operating principle of a PC cavity spectrometer using (a) an array of sequentially tuned cavities or (b) a single dynamically-tunable cavity.

bus waveguide. The resolution of such a spectrometer is given by the spectral width of the frequency response of the individual elements, which is typically of the order of 10GHz. Conversely, the total number of resolvable spectral lines, that is, the number of resonators that can be used, is limited by their free spectral range, that is, the separation between adjacent resonant frequencies of the cavity. Note that, in practice, the total number of resonators is limited by the loss introduced by each element, e.g., the silicon waveguide, the PC waveguide, etc. The drawback of cascaded spectrometers is that they require additional optics to couple light into and out of the resonators, which increases the device size and complicates its operation. It is also challenging to fabricate a number of cavities with identical Q values precisely tuned to an array of specific resonant wavelengths. To overcome these difficulties, we propose high-resolution spectroscopy based on a single tunable high- Q silicon PC cavity that both emits into and is excited from the vertical direction, thus eliminating

the need for a bus waveguide entirely [Fig. 4.1(b)]. In addition, we demonstrate that such a cavity can readily be used to discriminate between the absorption spectra of different chemical species. Two gases are considered here, acetylene ($^{12}\text{C}_2\text{H}_2$) and hydrogen cyanide (H^{12}CN). These are commonly used as wavelength references, with strong absorption lines in the vicinity of 1530 nm. Both gases are used industrially, but hydrogen cyanide is highly toxic.

4.1 Optimization of an L-3 cavity for high Q

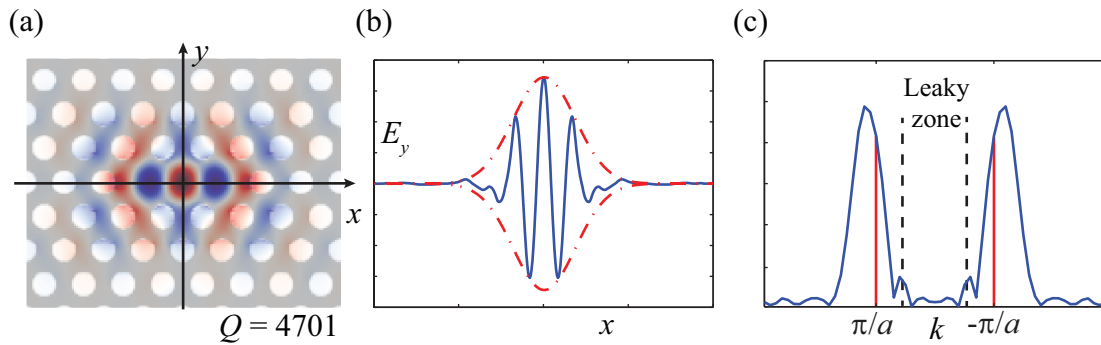


Figure 4.2: (a) Schematics of an intrinsic L-3 cavity and the electric field profile (E_y) of the fundamental resonant mode. The simulated Q factor is 4701. (b) The E -field distribution along the x -axis; (c) Spatial Fourier transform of the E -field in (b). Dashed lines show the boundary of the region where $|k| < \frac{2\pi}{\lambda_0}$ and λ_0 is the wavelength of light in vacuum.

The resolution of a cavity-based spectrometer is directly determined by the Q factor of the cavity. Intrinsic L-3 cavities typically have a Q value on the order

of 10^3 . Figure 4.2(a) shows the lattice structure of an intrinsic L-3 cavity and the electric field profile (E_y) of the resonant mode in the x - y plane. The simulated Q value is 4701. According to the physical meaning of the Q factor, this means that 0.02% of the entire stored energy is lost in each oscillation cycle. Since no material absorption, fabrication errors or wall roughness is considered in the simulation, out-of-plane emission is the principal loss mechanism. The E -field distribution along the x -axis can be approximated by a product of a sinusoidal function and an envelope function, as shown in Fig. 4.2(b). The spatial Fourier transform of the sinusoidal function produces two delta functions at $k = \pm\pi/a$ in the k -space, which are broadened by convolution with the Fourier transform of the envelope function and result in the spatial spectrum shown in Fig. 4.2(c). In the region $|k| < 2\pi/\lambda_0$ where “ λ_0 ” is the wavelength of light in air, TIR confinement in the z direction fails and light can escape through emission. Consequently, any abrupt change in the shape of the envelope function generates high frequency components in its Fourier transform and causes more light falls into the leaky zone. It has been shown that by engineering the positions and sizes of the two inner air holes on the x -axis, the edge of the envelope function can be smoothed [54]. Figure 4.3(a) shows the schematics and resonant mode E_y -field of an L-3 cavity with two inner holes shifted by $0.15a$ outward where “ a ” is the lattice constant. The simulated Q factor is 38430, which indicates that 0.0026% of the stored energy is lost in each cycle. In the structure shown in Fig. 4.3(b), the two air holes are shifted by $0.164a$ and the radii are reduced to $0.214a$. The simulated

Q factor rises up to a value of 97646, or, 0.001% of the stored energy escapes the cavity in each cycle. The value of Q is sensitive to the sizes and positions of the two terminating air holes because they affect the envelope shape of the resonant mode profile the most.

4.2 Thermal effect on the optical properties of nanocavities

We have fabricated L3 PC cavities optimized for high Q factor. Additionally, the radii of selected holes surrounding the cavity are slightly increased to modify the cavity's far-field emission pattern, and thus facilitate coupling in the out-of-plane direction. These PC cavities were fabricated on commercial silicon-on-insulator wafers (SOITEC). The patterns were defined by electron-beam lithography on a positive-tone resist (ZEP 520), and transferred to the Si membrane by inductively-coupled plasma etching. After removal of the remaining resist, the buried oxide layer was undercut by wet chemical etching. A scanning-electron micrograph of one such cavity is shown in Fig. 4.4(a). The fabricated cavities are characterized using resonant-scattering spectroscopy [71]. In our experimental setup [Fig. 4.4(b)], the cavity axis is oriented at a 45° angle with respect to the polarization of the incident light, which is set by a half-wave plate and a polarizer. A second polarizer, oriented at a 90° angle with respect to the incident polarization, controls the polarization of light that

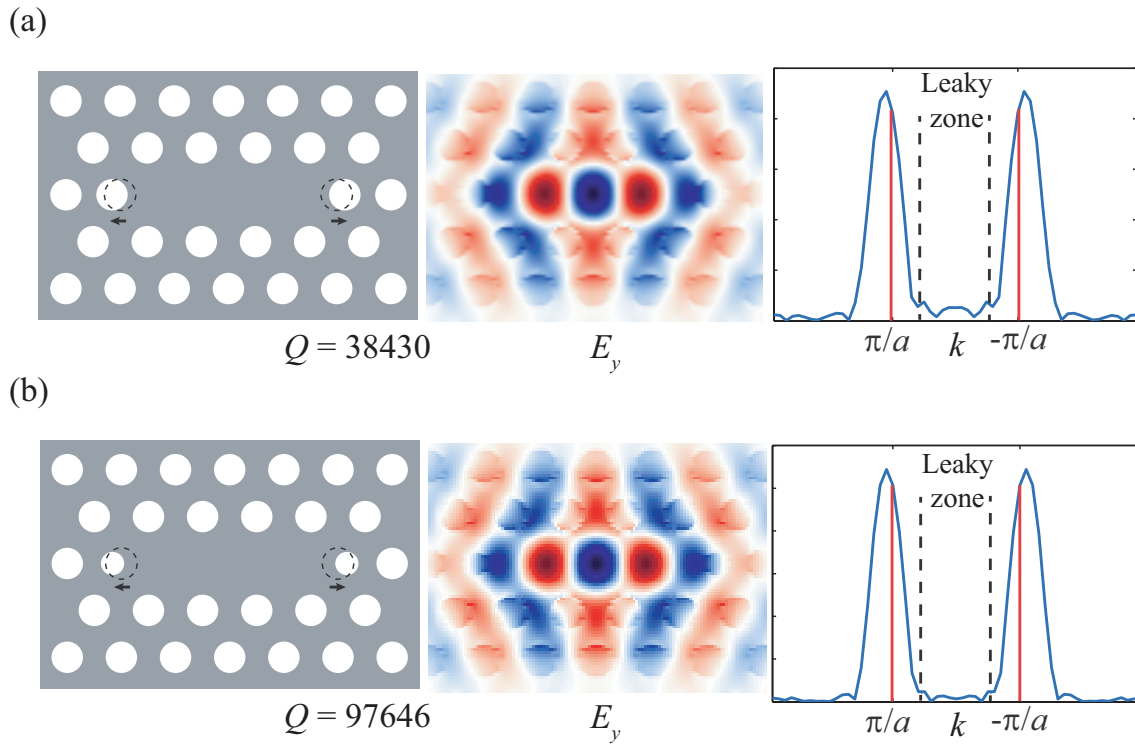


Figure 4.3: (a) Schematics of an L-3 cavity with the inner two air holes moved outward by an amount of $0.15a$. In the Fourier domain, less light falls into the leaky zone. The simulated Q factor is 38430. (b) The two inner holes are moved by $0.164a$ and their radii are reduced to $0.214a$. The simulated Q factor is 97646, more than 20 times higher than the intrinsic L-3 cavity.

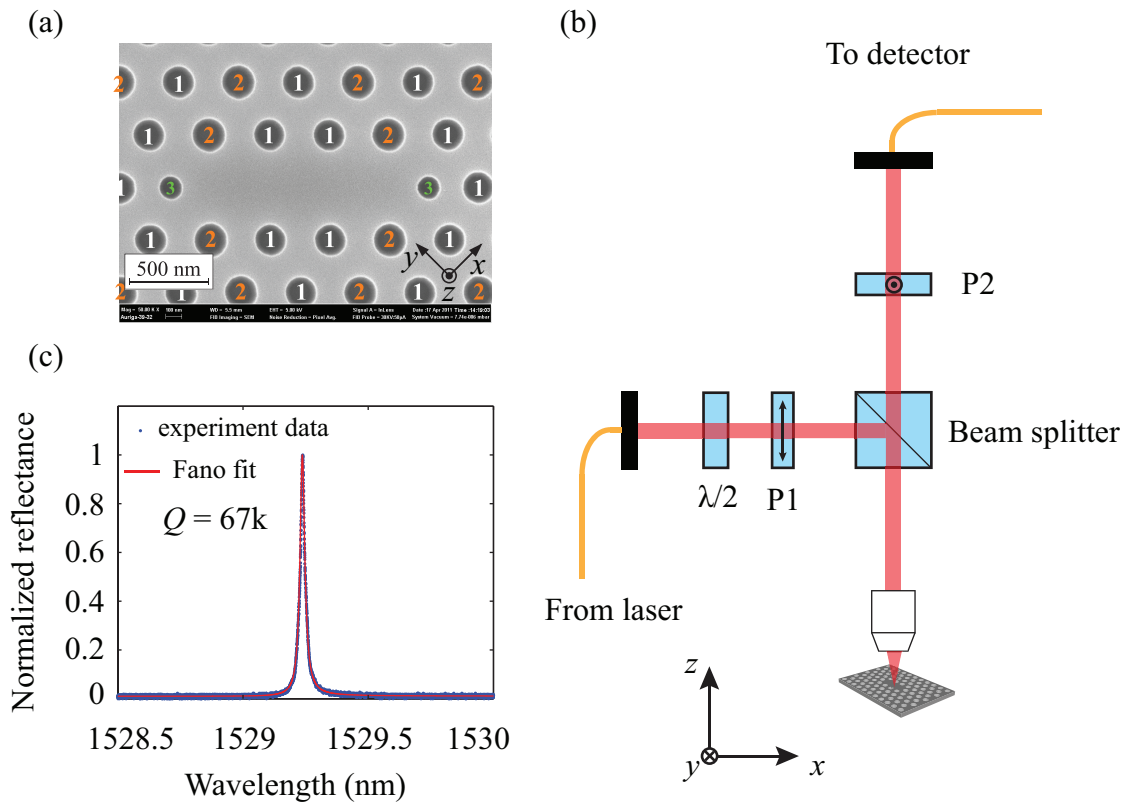


Figure 4.4: (a) Scanning-electron micrograph of an L-3 PC cavity optimized for vertical out-coupling. The holes are labeled according to their design radii. In this example, $r_1 = 89$ nm, $r_2 = 93$ nm, $r_3 = 62$ nm. Additionally, the holes labeled “3” are shifted outwards by 62 nm. (b) Schematic of the setup used to characterize PC cavities via resonant scattering. P1 and P2: crossed polarizers, $\lambda/2$: half-wave plate. Note that the light incident on the PC cavity is x-polarized, and that only light that is y-polarized is being collected by the detector. (c) Measured resonance of a typical L-3 PC cavity, displaying a Q of $\sim 6.7 \times 10^3$.

reaches the detector. As a result of this arrangement, stray light reflected from the sample surface is suppressed, and only light that has scattered resonantly through the cavity is collected. The resonantly-scattered intensity can then be fit with a Fano lineshape, from which we extract the resonant wavelength λ_0 and quality factor Q of the cavity [72]. For a typical cavity, Q is approximately 6.7×10^3 [Fig. 4.4(c)].

To examine the dependence of the resonant wavelength on temperature, a heating element is attached to the sample mounting block. The temperature is monitored with a thermocouple and is stabilized using a proportional-integral-derivative feedback circuit. At each temperature point we record the resonant wavelength λ_0 and coupling efficiency η , which is given by the ratio of scattered to incident optical power. A linear dependence of λ_0 on temperature is observed, with a slope of $0.07 \text{ nm}/^\circ\text{C}$ (Fig. 4.5), which is consistent with what one would expect based on the temperature dependence of the refractive index of silicon [73]. In the present demonstration we limit ourselves to operating temperatures near room temperature in order to avoid thermal gradients across the sample holder, which would render the thermometry inaccurate. The useful tuning range is approximately 1.5 nm for a temperature range of $20 \text{ }^\circ\text{C}$. The cavity Q -factor remains constant within 5% over this tuning range. In principle, this range could be extended by improved thermo-engineering design.

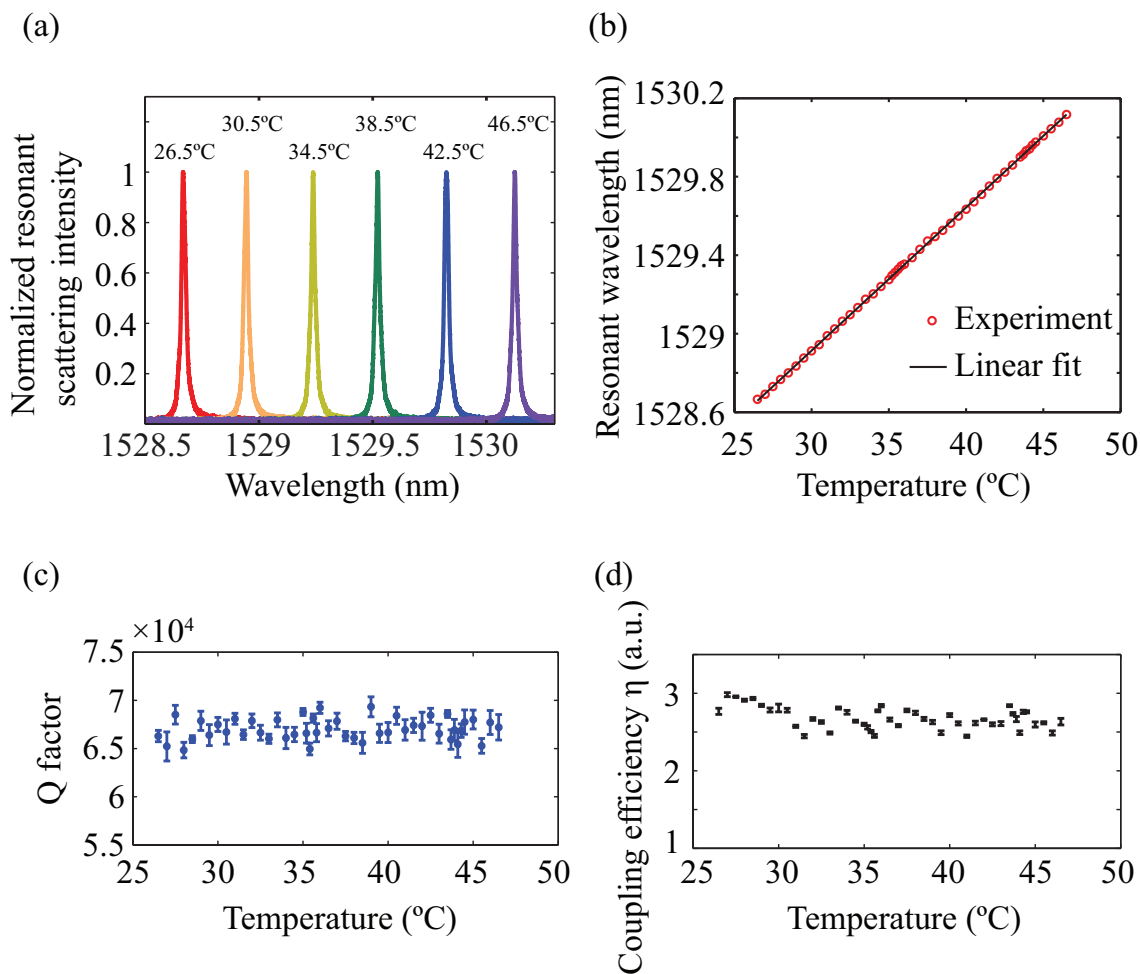


Figure 4.5: (a), Resonance peaks of the fabricated L-3 cavity at different temperatures; (b) Resonant wavelength versus temperature. The linear fit gives an estimated slope of 0.07 nm/°C. A tuning range of 1.4 nm is demonstrated. (c) Q factor at different temperatures and (d), coupling efficiency η as functions of temperature.

4.3 Spectrum differentiation of acetylene and hydrogen cyanide using a thermally tuned PC nano-cavity

Once characterized, the cavity can be used to perform spectroscopy with a spectral resolution of 0.02 nm (or, equivalently, 3 GHz or 0.1 wavenumbers at a wavelength range near 1550 nm), which is comparable to the resolution of a tabletop spectrometer. The cavity is illuminated with the absorption spectrum we wish to measure, and the optical power scattered by the cavity is recorded as the temperature of the chip is tuned. In our experiment [Fig. 4.6(a)], the spectra are generated by passing laser light through commercial fiber-coupled gas cells (Wavelength References Inc) that contain different chemical species: a 5.5-cm long cell filled with acetylene to a pressure of 740 Torr, and a 16.5-cm-long cell filled to 150 Torr with hydrogen cyanide. In order to emulate broad-band illumination we sweep the tunable laser over the wavelength range 1528.5 – 1530.2 nm, which covers lines P6 – P8 of acetylene and R5 – R7 of hydrogen cyanide, and integrate the detected signal at each wavelength to obtain the total scattered optical power O . Figure 4.6(b) shows the spectra measured using the PC cavity, which are given by the ratio of the scattered optical power to the coupling efficiency O/η . Note that the alternating strength of the absorption lines seen in the spectrum of acetylene is due to the triple degeneracy of the antisymmetric rotational levels of this linear symmetric molecule, which is a result of the nuclear moments

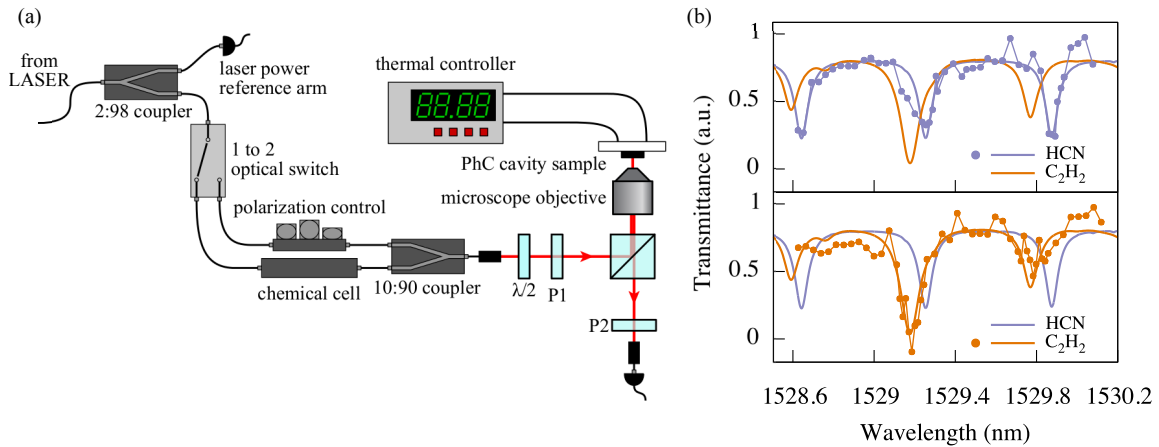


Figure 4.6: (a), Schematic of the setup used for spectroscopic measurements. (b), Measured transmission spectra of the hydrogen cyanide (top) and acetylene (bottom) gas cells. The transmission of the two gas cells, measured using a tunable laser, is also shown (solid lines). Note that the spectral resolution is adequate to discriminate between the two gases.

$I_H = 1/2$ and $I_C = 0$. Hydrogen cyanide, which is linear but not symmetric, does not display such an intensity alternation.

We see that the resolution of our cavity spectrometer is adequate to resolve neighboring absorption lines of acetylene and hydrogen cyanide. In principle, even better performance could be achieved by carefully optimizing the design of the PC cavities to further increase their quality factor. Similar cavities were recently demonstrated with Q factors exceeding two million [53]. Note, however, that in our current setup, the spectral resolution is limited not only by the cavity Q , but also by the stability of the thermal controller.

It is worth noting that by using a bus waveguide and multiple resonators, one could in principle perform parallel monitoring to decrease the data acquisition time. However, to construct a spectrometer of this type, we would need to fabricate a series of cavities whose resonances are equally spaced and span the target spectral range. The quality factor and resonant wavelength of PC cavities can be chosen by appropriately tuning the design parameters, but not with arbitrary precision. Control is ultimately limited by the inherent imperfections of the fabrication process. Unavoidable imperfections in the resulting structure, such as sidewall roughness and lithographic inaccuracies, lead to variations in resonant frequency even among nominally identical cavities [74]. These variations become more pronounced for high- Q cavities, for which the uncertainty in resonant wavelength can be much larger than their resonance linewidth. As a result, unless these variations are corrected for, fabrication disorder limits the practical resolution of the spectrometer, as one is confined to using low- Q cavities only. Even though multiple techniques have been demonstrated [75–79], controllable post-fabrication tuning of individual PC cavities remains a technical challenge.

5 Coupled-cavity waveguides with ultra wide-band slow-light

5.1 Enhancement of the spectral sensitivity of a Mach-Zehnder interferometer (MZI) by slow-light

In the field of spectroscopy, interferometry has found many applications including stabilization of laser wavelength, Fourier transform spectroscopy, etc. Enhanced-sensitivity interferometers have been an important subject of interest in the photonics community [59–61]. Figure 5.1(a) shows the schematics of a MZI. Assume the arm length difference between the two arms is L , the transmitted power at out-put port 1 takes on the form:

$$I(\omega) = \frac{1}{2}I_0 \left[1 + \cos\left(\frac{\omega L}{c}\right) \right], \quad (5.1)$$

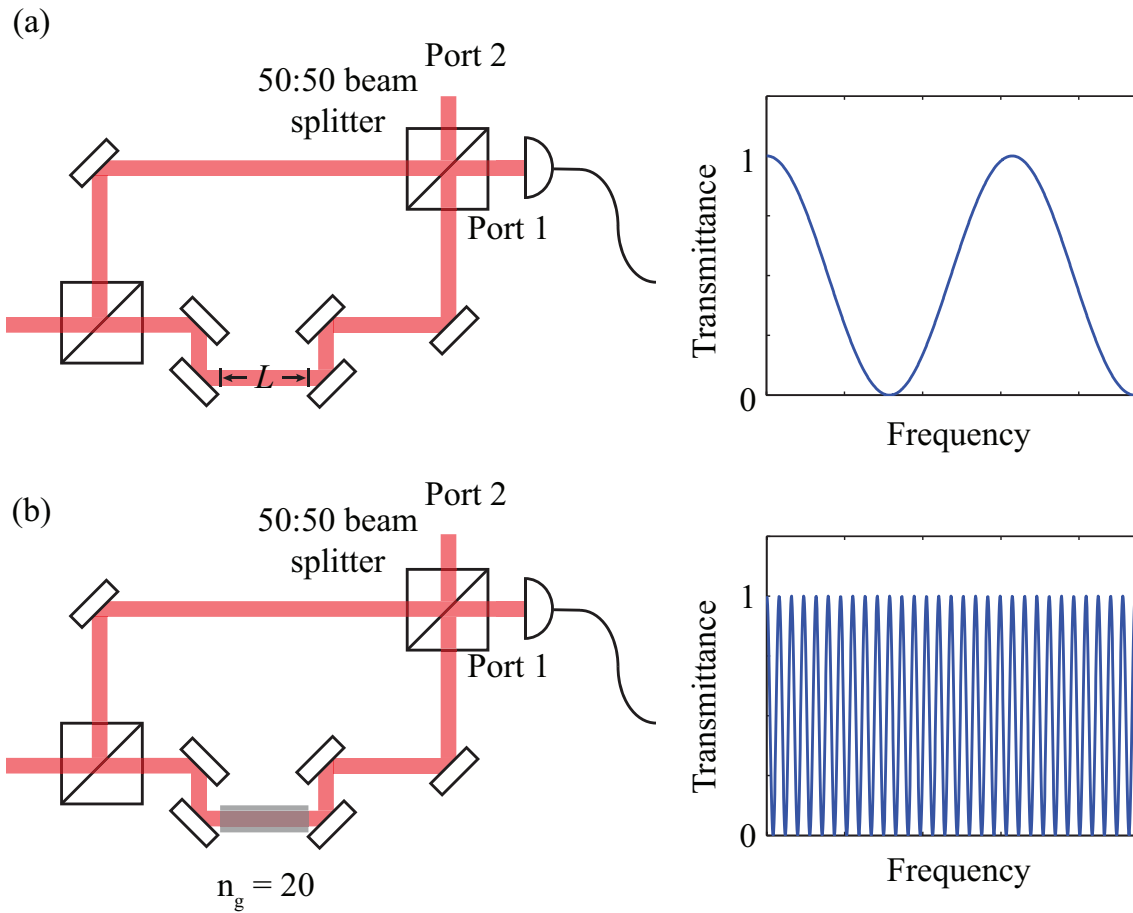


Figure 5.1: (a), Schematics of a MZI with an arm length difference of L and the transmittance as a function of frequency; (b), A slow-light material is inserted in one arm of the MZI. The transmittance profile shows a spectral sensitivity enhanced by a factor of the group index of the slow-light material.

where I_0 and ω are the intensity and frequency of the input light, respectively. The spectral sensitivity can be described by:

$$\frac{dI(\omega)}{d\omega} = -\frac{I_0 L}{2c} \sin\left(\frac{\omega L}{c}\right). \quad (5.2)$$

Equation 5.2 suggests that the spectral sensitivity of a MZ interferometer is proportional to its arm length difference, which poses a lower limit to the size of the entire device. However, if the arm length difference is provided by a piece of slow-light material with a group index n_g as shown in Fig. 5.1(b), the transmitted power is:

$$I(\omega) = \frac{1}{2} I_0 \left[1 + \cos\left(\frac{n(\omega)\omega L}{c}\right) \right] \quad (5.3)$$

where $n(\omega)$ is the frequency dependent refractive index of the slow-light material.

The spectral sensitivity in this case is

$$\frac{dI(\omega)}{d\omega} = -\frac{I_0 L}{2c} \sin\left(\frac{\omega L}{c}\right) \left[n(\omega) + \omega \frac{dn(\omega)}{d\omega} \right] = -n_g \frac{I_0 L}{2c} \sin\left(\frac{\omega L}{c}\right). \quad (5.4)$$

Compared to Eq. 5.2, the spectral sensitivity is enhanced by a factor of n_g . This is also shown in the transmittance versus frequency plot in Fig. 5.1(b) where the fringe density is 20 times as high as that from an intrinsic MZI. Therefore, slow-light materials can be used to enhance the spectral sensitivity of interferometers without increasing the physical size of the device.

The improvement of the spectral sensitivity of interferometers has been demonstrated in bulk optical setups, such as shearing and free-space interferometers, with highly dispersive crystals and atomic vapors [59–61]. While not achieving the same

extreme slowdown values as material slow light, slow-light in nanophotonic devices has many key advantages. Nanophotonic slow-light structures are extremely compact, with low footprint and high mechanical stability, compared to material slow-light systems [80,81]. We have fabricated slow-light PC waveguides and constructed a compact fiber MZI with the slow-light waveguide in one arm. The waveguide has a lattice constant of 416 nm and a hole radius of 124 nm. The silicon slab is 210 nm thick, and the first and second rows are shifted by 46 nm outward and 16 nm inward, respectively, as shown in Fig. 5.2(a). Figure 5.2(b) shows the the schematics of the fiber based MZI. Light is coupled into and out of the waveguide using grating couplers etched at the same time as the PC waveguide [82–84]. The intensity of the output of the slow-light MZ interferometer is measured as a function of wavelength through use of an optical spectrum analyzer (OSA). We use a broadband, amplified spontaneous emission (ASE) source spanning the wavelength range from 1525 nm to 1575 nm. These results are shown in Fig. 5.2(c)-(f). The increase in fringe density with wavelength is a consequence of the slow light effect produced by the dispersive properties of the PhC waveguide. Compared to an interferometer without any slow-light material inserted, our proof-of-principle device shows that its sensitivity can be increased by a factor as large as 20, as shown in Fig. 5.3.

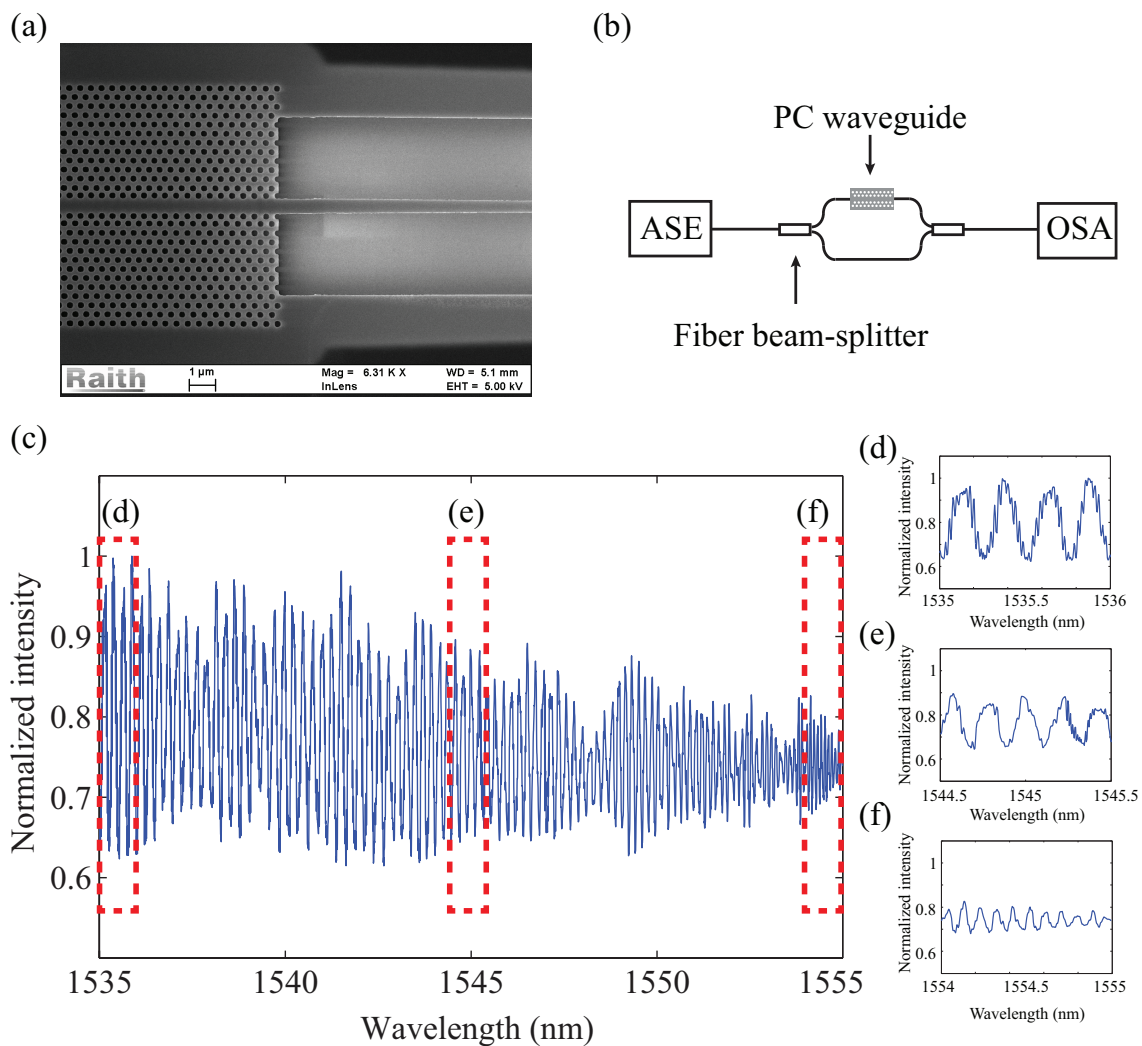


Figure 5.2: (a), Scanning electron microscope (SEM) photograph of the fabricated PC waveguides with its input channel; (b), Fiber based MZI containing a PC slow-light waveguide in one of the arms; (c), Interference fringes as a function of wavelength measured by the OSA; (d)-(f), Three different 1 nm spans with significantly different fringe spacings.

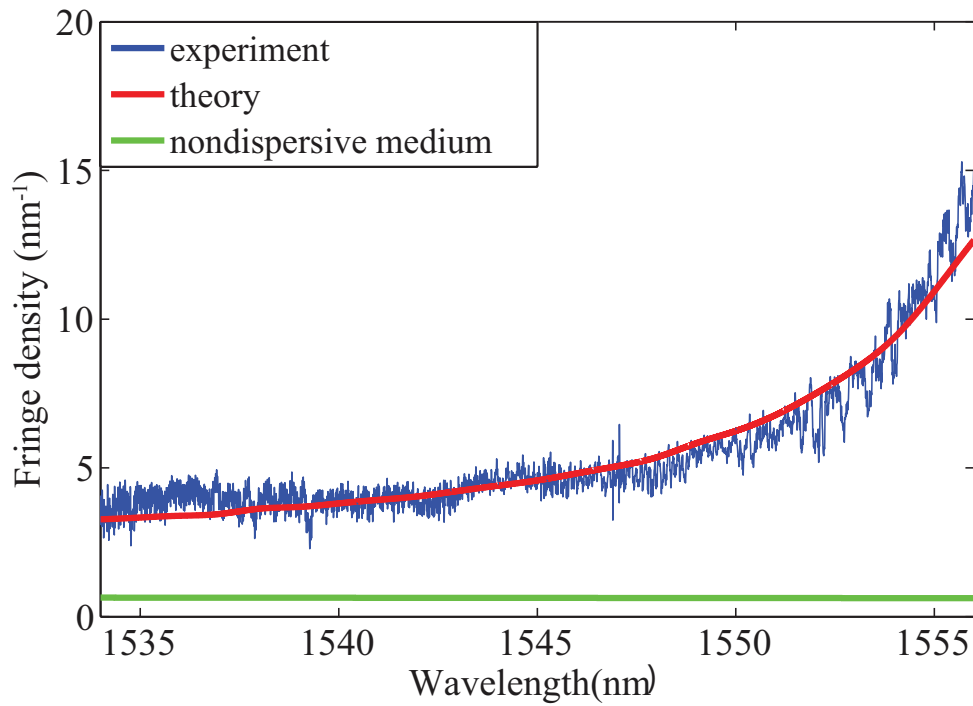


Figure 5.3: Experimental measurements and theoretical predictions of the density of interference fringes plotted as a function of wavelength for the slow-light MZ interferometer of Fig. 5.2(b). The green curve is the simulated fringe density of the MZI when the slow-light waveguide is replaced by free space of the same length.

5.2 Design of a wide-band slow-light coupled-cavity waveguide (CCW)

The slow-light PC waveguide studied in the previous section shows a slow-light region of roughly 5 nm in spectral bandwidth. However, the group index is not constant within this region. In an effort to realize wide-band slow-light operations in chip-scale photonic devices and achieve a near constant spectral sensitivity over the slow-light bandwidth, we propose a CCW design [85] shown in Fig. 5.4(a). One unit cell of such a CCW is composed of two L3 cavities separated by $5a$ in the x -direction and $\sqrt{3}a$ in the propagation direction y , where “ a ” is the lattice constant of the PC. As discussed in section 1.4, to achieve a large group index, a high $\Delta k/\Delta\omega$ ratio is desirable. By employing a staggered geometry, the short spatial period in the y -direction results in a large Brillouin zone in k space. Radii of red and green air holes are modified (Δr_1 and Δr_2 respectively) to lower the first- and second-neighbor couplings, resulting a smaller $\Delta\omega$. To reduce emission loss, radii and positions of the blue air holes (Δr_3 and Δx respectively) are modified with respect to the PC bulk air holes to increase the Q of each L3 cavity. Figure 5.4(b) shows the top view scanning electron microscope image of one CCW composed of 50 cavities (50-CCW) fabricated in silicon-on-insulator. The CCWs is coupled to two separate input-output PC waveguides (red arrows in Fig. 5.4(b)) each of which is butt-coupled to a silicon-strip waveguide for end-fire coupling.

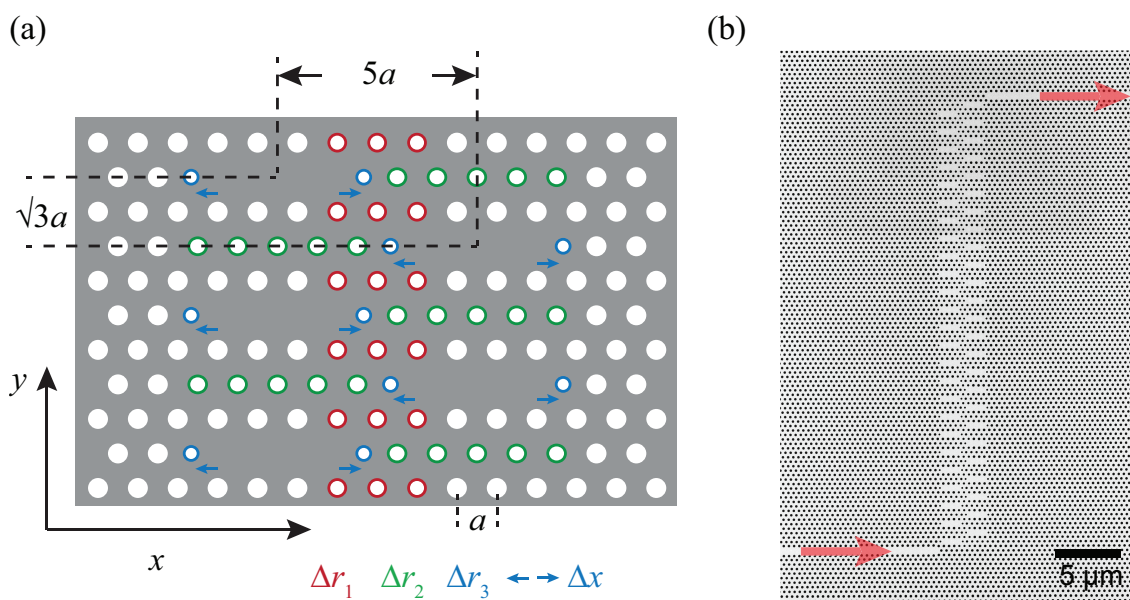


Figure 5.4: (a), Schematic diagram of the CCW design. (b), SEM top view picture of a 50-CCW. Red arrows indicate the input and output of light in the PC waveguides.

5.3 Experimental study of CCWs' slow-light performance

The slow-light characteristics of the CCWs were determined through Fourier transform spectral interferometry [86]. Figure 5.5(a) shows the schematics of the experiment setup. The polarization of light from a tunable laser was controlled by a manual fiber polarization controller. A 1-to-2 fiber coupler separated the input light into two arms. One arm (arm A) was composed of a CCW chip and two pieces of tapered fibers for input/output coupling, while the other arm (arm B) was a single piece of SMF-28 fiber serving as a reference arm. Light from the two arms was combined by a 2-to-1 fiber coupler and a power meter was used to record the output intensity as a function of laser frequency.

We first scanned the laser frequency when no CCW chip was present in arm A and the tapered fibers were directly coupled to each other by placing the tips close together. The total fiber length in arm B was approximately 6 cm longer than that in arm A. This path length difference lead to a relative phase “ $\varphi_{r0}(\omega)$ ” between light in the two arms. The normalized transmitted intensity of the MZI in a small frequency range from $\omega_1 = 1.2078879 \times 10^{15} \text{ rad/s}$ to $\omega_2 = 1.2079653 \times 10^{15} \text{ rad/s}$ is shown in Fig. 5.5(b). Between two adjacent maxima (minima) of the oscillations, $\varphi_{r0}(\omega)$ changes by an amount of 2π . Consequently, one can calculate $\varphi_{r0}(\omega)$ from the intensity profile $I(\omega)$. Figure 5.5(c) shows the phase shift $\varphi_{r0}(\omega) - \varphi_{r0}(\omega_1)$ inside

the same frequency range. Without changing the length of arm B, the tapered fibers in arm A were moved apart and a CCW chip was inserted in between. The laser frequency was tuned and the interference pattern was recorded to find the relative phase $\varphi_r(\omega)$. The difference between the relative phases $\varphi_{r0}(\omega)$ and $\varphi_r(\omega)$ was caused by adding the CCW chip to the MZI. We assume that the integrated input/output waveguides on the CCW chip have an effective index of $n_{\text{wg}}(\omega)$ and a total length of L_{wg} , and the CCW has an effective index of $n_{\text{ccw}}(\omega)$ and a length of L_{ccw} , the CCW chip contributes a phase shift of $\varphi_{\text{chip}}(\omega) = \omega n_{\text{ccw}}(\omega)L_{\text{ccw}}/c + \omega n_{\text{wg}}(\omega)L_{\text{wg}}/c$ to arm A, where “ c ” is the speed of light in vacuum. It follows that

$$\begin{aligned}\omega n_{\text{ccw}}(\omega)L_{\text{ccw}}/c &= \varphi_{\text{chip}}(\omega) - \omega n_{\text{wg}}(\omega)L_{\text{wg}}/c \\ &= \varphi_r(\omega) - \varphi_{r0}(\omega) - \omega n_{\text{wg}}(\omega)L_{\text{wg}}/c.\end{aligned}\quad (5.5)$$

Take derivative with respect to ω on both sides, equation 5.5 becomes:

$$n_{g\text{ccw}}(\omega)L_{\text{ccw}}/c = d[\varphi_r(\omega) - \varphi_{r0}(\omega)]/d\omega - n_{g\text{wg}}(\omega)L_{\text{wg}}/c, \quad (5.6)$$

where $n_{g\text{ccw}}(\omega) = n_{\text{ccw}}(\omega) + \omega dn_{\text{ccw}}(\omega)/d\omega$ is the group index of the CCW and $n_{g\text{wg}}(\omega) = n_{\text{wg}}(\omega) + \omega dn_{\text{wg}}(\omega)/d\omega$ the group index of the on-chip waveguides. $\varphi_r(\omega)$ and $\varphi_{r0}(\omega)$ can be measured experimentally and the length of both the CCW and on-chip waveguides are known design parameters. By measuring CCWs of two different lengths with identical on-chip coupling waveguide designs, the term $n_{g\text{wg}}(\omega)L_{\text{wg}}/c$ can be calibrated and the group index of the CCW can be calculated as:

$$n_{g\text{ccw}}(\omega) = \frac{c}{L_{\text{ccw}}}d[\varphi_r(\omega) - \varphi_{r0}(\omega)]/d\omega - n_{g\text{wg}}(\omega)\frac{L_{\text{wg}}}{L_{\text{ccw}}}\quad (5.7)$$

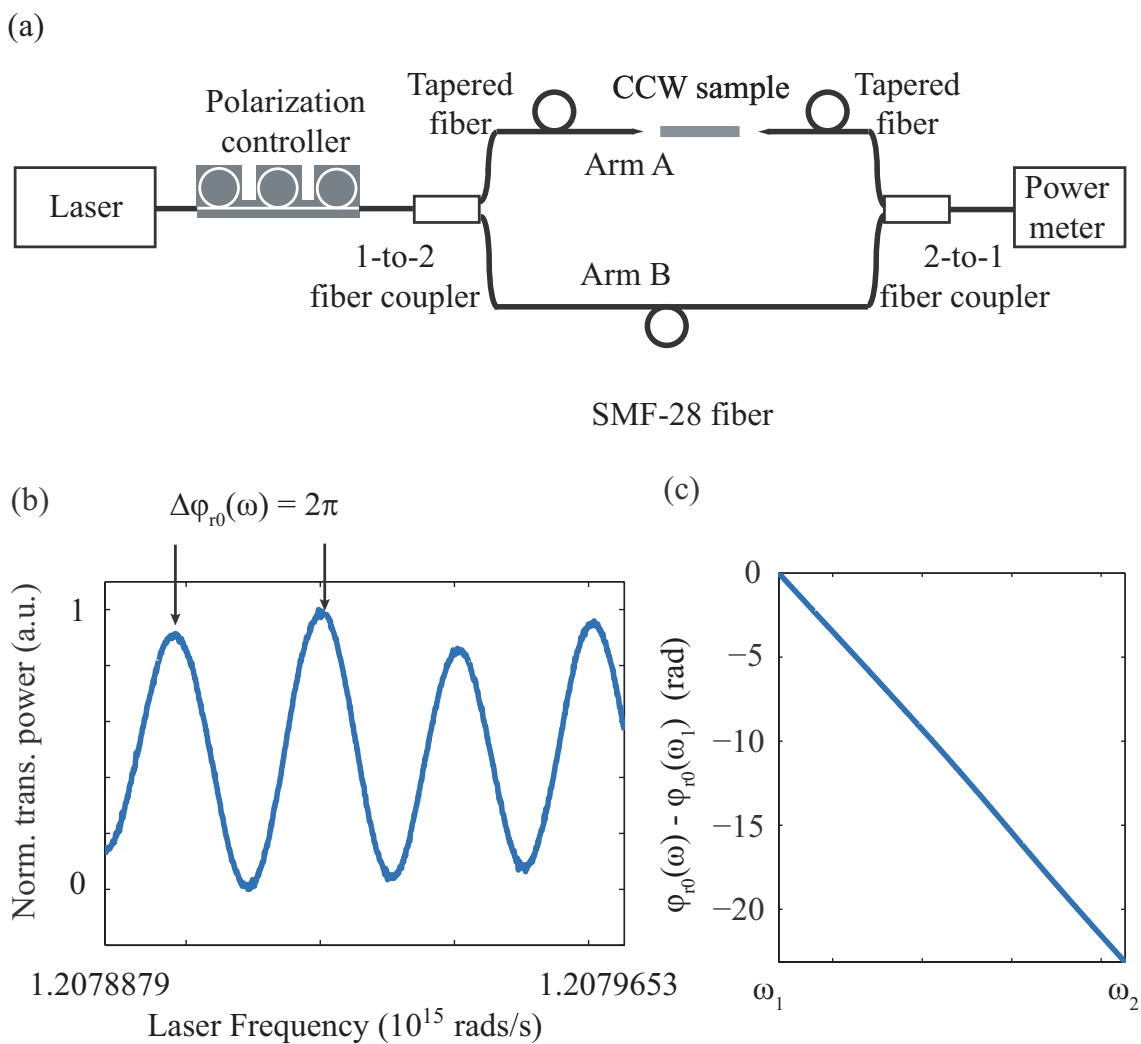


Figure 5.5: (a), Schematics of the experiment setup. (b), Normalized transmitted intensity as a function of laser frequency. (c), Relative phase change calculated from (b).

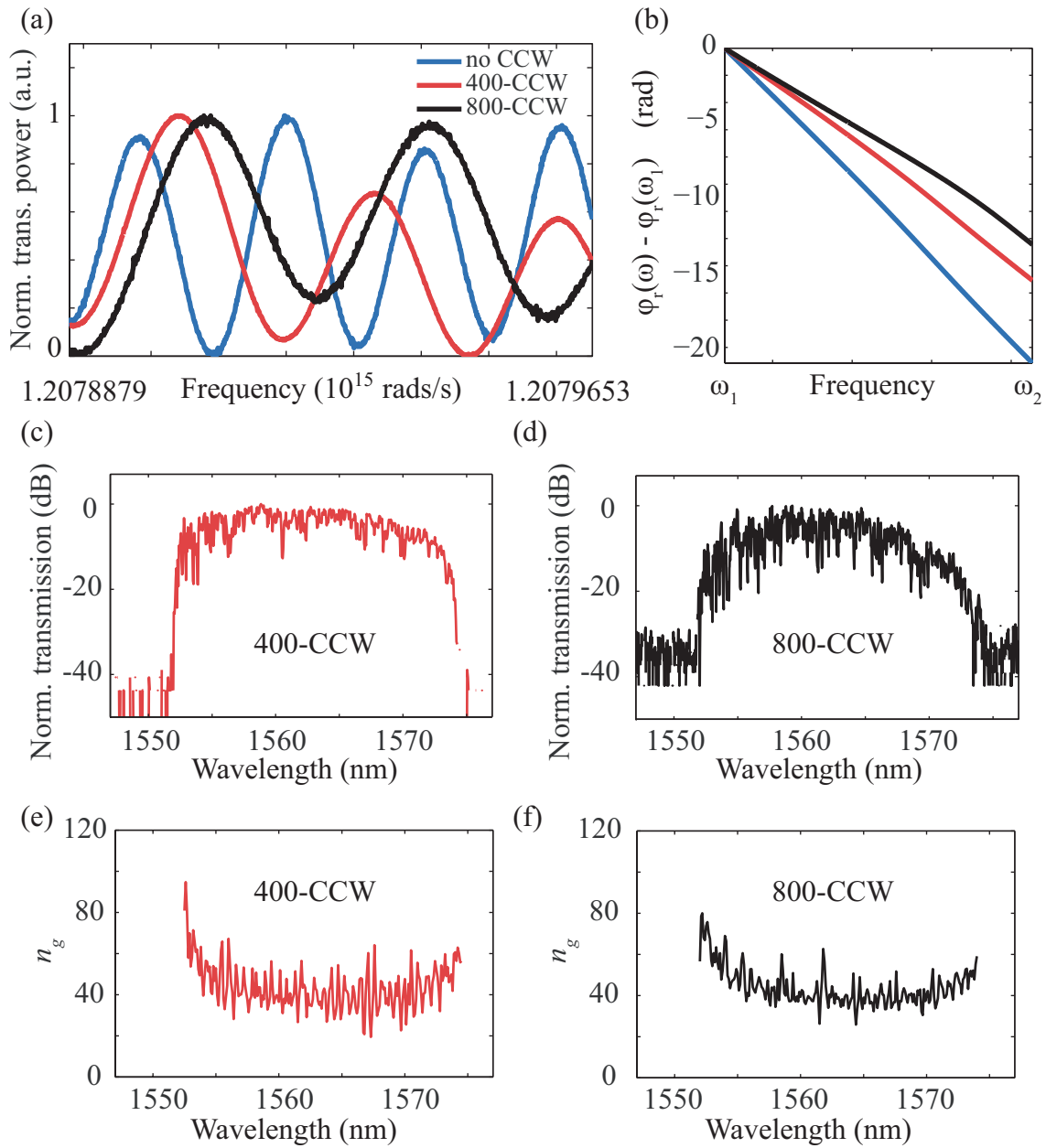


Figure 5.6: (a), Normalized transmitted intensity when there is no CCW, a 400-CCW and a 800-CCW in the MZI, respectively.(b), Relative phase calculated from (a). (c),(d), Transmission profiles of the CCWs. (e),(f), Group indices of the CCWs as a function of wavelength calculated from equation 5.7. The noise is mainly due to laser sweeping wavelength error.

The measured interference patterns of a CCW composed of 400 cavities (400-CCW) and a CCW of 800 cavities (800-CCW) are shown in Fig. 5.6(a). In comparison, the curve in Fig. 5.5(b) is also plotted in the same frequency range. Figure 5.6(b) shows the relative phase change calculated from (a). By blocking the reference arm (arm B), we also measured the transmission characteristics of the CCWs as shown in Fig. 5.6(c) and (d). The group indices of the CCWs calculated from equation 5.7 are shown in Fig. 5.6(e) and (f). Both of the CCWs have a group index around 40 over a 18 nm wide wavelength range. As predicted by Ref. [85], our results show that the designed CCWs have achieved wide-band slow-light operations. It is worth noting that in our experiment, the wavelength sweeping of the external cavity tunable laser was not strictly linear and precise at all wavelengths, due to equipment imperfections. The oscillating noise in the calculated group indices was caused by this equipment error and can be reduced by using a high precision laser.

6 Conclusions and future works

In this thesis, I have reviewed my study on several PC structures for miniature spectrometer designs. Chapter 1 introduced background information of the superprism effect, L-3 PC nano-cavities and CCWs. In chapter 2 and 3, theoretical and experimental studies of a flat-band superprism structure were discussed. Our findings confirmed that PC superprism structures can be optimized to better function as a spectrometer. Further optimization can be made by testing the effect of elliptical air holes and their orientations with respect to the basis vectors.

As mentioned in section 3.2, when designing a commercial spectrometer product using our optimization method, one can perform the simulations with much higher resolutions in 3-D space and in the parameter space to find superior designs. Nonetheless, the total number of working channels shown in our result exceeded the previously reported record by 50% [46, 48].

Multiple superprism structures with difference preconditioning distances were fab-

ricated when we conducted the experiment described in section 3.2. Several samples with promising lattice geometry designs suffered from broken output waveguides that did not survive the under etching process. This can be fixed by repeating the fabrication with a different concentration of HF and immersion time for under etching.

As a proof of concept, we used an infrared camera to collect the scattered light. A drawback of this configuration is that the in-plane scattered light from the end of one waveguide can be scattered out of the plane by the end of a neighboring waveguide. This increased the crosstalk level in our result. The measured power was also affected by the pixel size and dynamic range of the camera. In future experiments, the length of the output waveguide can be increased to enable end fire coupling for transmitted signal. This can increase the accuracy of the experiment and lower the crosstalk. With these improvements, we expect even more working channels can be achieved based on our design.

In addition, coupling efficiency of light from the preconditioning area into the PC region can be increased by engineering the shape of the interface air holes [87], as shown in Fig. 6.1(a), or adiabatic transition of the air hole radii at the PC edge [88,89], as shown in Fig. 6.1(b).

Chapter 4 demonstrated a spectrometer design based on thermally tuned single L-3 PC cavity with a high Q value. In our experiment, the L-3 cavity is fabricated on a 1 cm-by-1 cm SOI chip. In the thermal tuning process, the entire chip is placed on a heater. In real applications, the size of the device can be reduced by directly

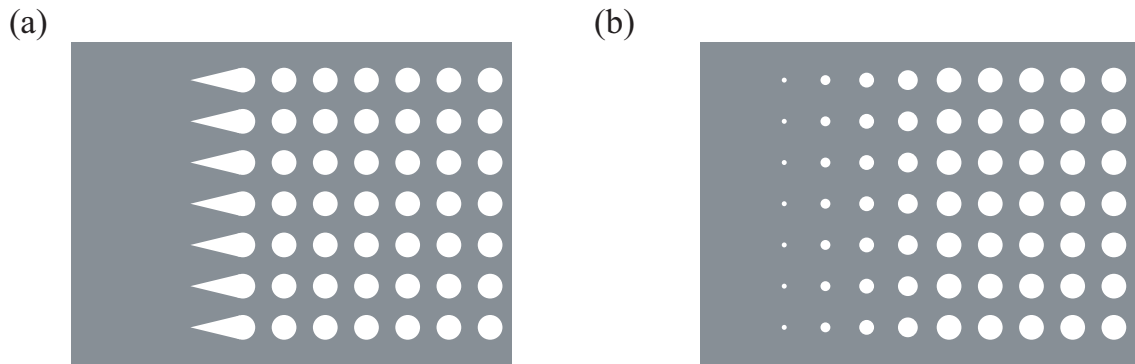


Figure 6.1: (a), Specially engineered interface hole shape for high efficiency coupling. (b), Adiabatic transition of hole radii near the edge of the PC area.

depositing on-chip metal heaters near the cavity. The resolution of such a spectrometer can be further improved by increasing the Q factor of the cavity used through carefully engineering the radii and positions of the inner air holes.

Chapter 5 reported our study on slow-light interferometry. Specifically, we have demonstrated a wide-band slow-light CCW on a SOI platform. The next recommended effort may focus on introducing a tuning mechanism for the magnitude of the slow-light effect in the CCWs for developing an integrated version of the slow-light Fourier transform interferometer reported by Ref. [60].

Bibliography

- [1] I. Newton, *Opticks:: Or, A Treatise of the Reflections, Refractions, Inflections and Colours of Light*. London : Printed for William Innys at the West-End of St. Paul's, 1730.
- [2] M. Czerny and A. F. Turner, "Über den astigmatismus bei spiegelspektrometern," *Zeitschrift für Physik*, vol. 61, no. 11, pp. 792–797, Nov 1930. [Online]. Available: <http://dx.doi.org/10.1007/BF01340206>
- [3] J. W. Goodman, *Introduction to Fourier Optics*. Roberts & Company Publishers, 2005.
- [4] P. Krippner, J. Mohr, C. Mueller, and C. van der Sel, "Microspectrometer for the infrared range," pp. 277–282, 1996. [Online]. Available: <http://dx.doi.org/10.1117/12.248496>
- [5] P. D. Trinh, S. Yegnanarayanan, F. Coppinger, and B. Jalali, "Silicon-on-insulator (soi) phased-array wavelength multi/demultiplexer with extremely low-polarization sensitivity," *IEEE Photonics Technology Letters*, vol. 9, no. 7, pp. 940–942, July 1997.

- [6] M. R. Pearson, A. Bezinger, A. Delage, J. W. Fraser, S. Janz, P. E. Jessop, and D.-X. Xu, "Arrayed waveguide grating demultiplexers in silicon-on-insulator," pp. 11–18, 2000. [Online]. Available: <http://dx.doi.org/10.1117/12.379610>
- [7] J. H. Correia, M. Bartek, and R. F. Wolffenbuttel, "High-selectivity single-chip spectrometer in silicon for operation in visible part of the spectrum," *IEEE Transactions on Electron Devices*, vol. 47, no. 3, pp. 553–559, Mar 2000.
- [8] S.-H. Kong, J. H. Correia, G. de Graaf, M. Bartek, and R. F. Wolffenbuttel, "Integrated silicon microspectrometers," *IEEE Instrumentation Measurement Magazine*, vol. 4, no. 3, pp. 34–38, Sept 2001.
- [9] R. V. Kruzelecky and A. K. Ghosh, "High-performance miniature integrated infrared spectrometers for industrial and biochemical sensing," pp. 25–34, 2001. [Online]. Available: <http://dx.doi.org/10.1117/12.417457>
- [10] S. Kong, D. Wijngaards, and R. Wolffenbuttel, "Infrared micro-spectrometer based on a diffraction grating," *Sensors and Actuators A: Physical*, vol. 92, no. 1, pp. 88 – 95, 2001, selected Papers for Eurosensors XIV. [Online]. Available: <http://www.sciencedirect.com/science/article/pii/S0924424701005441>
- [11] Z. mei Qi, N. Matsuda, T. Yoshida, H. Asano, A. Takatsu, and K. Kato, "Optical waveguide spectrometer based on thin-film glass plates," *Opt. Lett.*, vol. 27, no. 22, pp. 2001–2003, Nov 2002. [Online]. Available: <http://ol.osa.org/abstract.cfm?URI=ol-27-22-2001>
- [12] J. T. Bradshaw, S. B. Mendes, and S. S. Saavedra, "Planar integrated optical

- waveguide spectroscopy,” *Analytical Chemistry*, vol. 77, no. 1, pp. 28 A–36 A, 2005. [Online]. Available: <http://dx.doi.org/10.1021/ac053303q>
- [13] P. Cheben, “Wavelength dispersive planar waveguide devices: echelle gratings and arrayed waveguide gratings,” in *Optical Waveguides: from Theory to Applied Technologies*, M. L. Calvo and V. Lakshminarayanan, Eds. London: CRC Press, 2007, ch. 5.
- [14] P. Cheben, J. H. Schmid, A. Delâge, A. Densmore, S. Janz, B. Lamontagne, J. Lapointe, E. Post, P. Waldron, and D.-X. Xu, “A high-resolution silicon-on-insulator arrayed waveguide grating microspectrometer with sub-micrometer aperture waveguides,” *Opt. Express*, vol. 15, no. 5, pp. 2299–2306, Mar 2007. [Online]. Available: <http://www.opticsexpress.org/abstract.cfm?URI=oe-15-5-2299>
- [15] K. Ohtaka, “Energy band of photons and low-energy photon diffraction,” *Phys. Rev. B*, vol. 19, pp. 5057–5067, May 1979. [Online]. Available: <https://link.aps.org/doi/10.1103/PhysRevB.19.5057>
- [16] E. Yablonovitch, “Inhibited spontaneous emission in solid-state physics and electronics,” *Phys. Rev. Lett.*, vol. 58, pp. 2059–2062, May 1987. [Online]. Available: <http://link.aps.org/doi/10.1103/PhysRevLett.58.2059>
- [17] S. John, “Strong localization of photons in certain disordered dielectric superlattices,” *Phys. Rev. Lett.*, vol. 58, pp. 2486–2489, Jun 1987. [Online]. Available: <http://link.aps.org/doi/10.1103/PhysRevLett.58.2486>

- [18] E. Yablonovitch, “Photonic band-gap structures,” *J. Opt. Soc. Am. B*, vol. 10, no. 2, pp. 283–295, Feb 1993. [Online]. Available: <http://josab.osa.org/abstract.cfm?URI=josab-10-2-283>
- [19] J. D. Joannopoulos, P. R. Villeneuve, and S. Fan, “Photonic crystals: putting a new twist on light,” *Nature*, vol. 386, pp. 143–149, Mar 1997. [Online]. Available: <http://dx.doi.org/10.1038/386143a0>
- [20] K. Inoue and K. Ohtaka, *Photonic Crystals*. Springer, 2004.
- [21] J. D. Joannopoulos, S. G. Johnson, J. N. Winn, and R. D. Meade, *Photonic Crystals, Molding the Flow of Light*. Princeton University Press, 2008.
- [22] J.-M. Lourtioz, H. Benisty, V. Berger, J.-M. Gerard, D. Meystre, and A. Tchel-nokov, *Photonic Crystals*. Springer, 2008.
- [23] E. Yablonovitch, T. J. Gmitter, and K. M. Leung, “Photonic band structure: The face-centered-cubic case employing nonspherical atoms,” *Phys. Rev. Lett.*, vol. 67, pp. 2295–2298, Oct 1991. [Online]. Available: <https://link.aps.org/doi/10.1103/PhysRevLett.67.2295>
- [24] P. R. Villeneuve and M. Piché, “Photonic band gaps in two-dimensional square and hexagonal lattices,” *Phys. Rev. B*, vol. 46, pp. 4969–4972, Aug 1992. [Online]. Available: <https://link.aps.org/doi/10.1103/PhysRevB.46.4969>
- [25] K. Ho, C. Chan, C. Soukoulis, R. Biswas, and M. Sigalas, “Photonic band gaps in three dimensions: New layer-by-layer periodic structures,” *Solid State Communications*, vol. 89, no. 5, pp. 413 – 416, 1994. [Online]. Available:

<http://www.sciencedirect.com/science/article/pii/003810989490202X>

- [26] L. R. S. R. S., “Xvii. on the maintenance of vibrations by forces of double frequency, and on the propagation of waves through a medium endowed with a periodic structure,” *Philosophical Magazine*, vol. 24, no. 147, pp. 145–159, 1887. [Online]. Available: <http://dx.doi.org/10.1080/14786448708628074>
- [27] E. Yablonovitch and T. J. Gmitter, “Photonic band structure: The face-centered-cubic case,” *Phys. Rev. Lett.*, vol. 63, pp. 1950–1953, Oct 1989. [Online]. Available: <https://link.aps.org/doi/10.1103/PhysRevLett.63.1950>
- [28] M. Notomi, “Theory of light propagation in strongly modulated photonic crystals: Refractionlike behavior in the vicinity of the photonic band gap,” *Phys. Rev. B*, vol. 62, pp. 10 696–10 705, Oct 2000. [Online]. Available: <https://link.aps.org/doi/10.1103/PhysRevB.62.10696>
- [29] R. A. Shelby, D. R. Smith, and S. Schultz, “Experimental verification of a negative index of refraction,” *Science*, vol. 292, no. 5514, pp. 77–79, 2001. [Online]. Available: <http://www.sciencemag.org/content/292/5514/77.abstract>
- [30] C. Luo, S. G. Johnson, J. D. Joannopoulos, and J. B. Pendry, “All-angle negative refraction without negative effective index,” *Phys. Rev. B*, vol. 65, p. 201104, May 2002. [Online]. Available: <https://link.aps.org/doi/10.1103/PhysRevB.65.201104>
- [31] E. Cubukcu, K. Aydin, E. Ozbay, S. Foteinopoulou, and C. M. Soukoulis, “Electromagnetic waves: Negative refraction by photonic crystals,” *Nature*, vol. 423,

- no. 6940, pp. 604–605, Jun 2003.
- [32] C. Luo, S. G. Johnson, J. D. Joannopoulos, and J. B. Pendry, “Negative refraction without negative index in metallic photonic crystals,” *Opt. Express*, vol. 11, no. 7, pp. 746–754, Apr 2003. [Online]. Available: <http://www.opticsexpress.org/abstract.cfm?URI=oe-11-7-746>
- [33] Z. Ruan, M. Qiu, S. Xiao, S. He, and L. Thylén, “Coupling between plane waves and bloch waves in photonic crystals with negative refraction,” *Phys. Rev. B*, vol. 71, p. 045111, Jan 2005. [Online]. Available: <https://link.aps.org/doi/10.1103/PhysRevB.71.045111>
- [34] K. Ohlinger, I. Olvera, and Y. Lin, “Negative refraction behaviors in two-dimensional elliptical-rod photonic crystals in a centered rectangular lattice,” *Journal of Applied Physics*, vol. 106, no. 2, p. 023516, 2009. [Online]. Available: <http://dx.doi.org/10.1063/1.3176947>
- [35] H. Kosaka, T. Kawashima, A. Tomita, M. Notomi, T. Tamamura, T. Sato, and S. Kawakami, “Self-collimating phenomena in photonic crystals,” *Applied Physics Letters*, vol. 74, no. 9, pp. 1212–1214, 1999. [Online]. Available: <http://dx.doi.org/10.1063/1.123502>
- [36] J. Witzens, M. Loncar, and A. Scherer, “Self-collimation in planar photonic crystals,” *Selected Topics in Quantum Electronics, IEEE Journal of*, vol. 8, no. 6, pp. 1246 – 1257, nov/dec 2002.
- [37] S.-Y. Lin, V. M. Hietala, L. Wang, and E. D. Jones, “Highly dispersive photonic

- band-gap prism,” *Opt. Lett.*, vol. 21, no. 21, pp. 1771–1773, Nov 1996. [Online]. Available: <http://ol.osa.org/abstract.cfm?URI=ol-21-21-1771>
- [38] H. Kosaka, T. Kawashima, A. Tomita, M. Notomi, T. Tamamura, T. Sato, and S. Kawakami, “Superprism phenomena in photonic crystals,” *Phys. Rev. B*, vol. 58, no. 16, pp. R10 096–R10 099, Oct 1998.
- [39] —, “Superprism phenomena in photonic crystals: Toward microscale lightwave circuits,” *J. Lightwave Technol.*, vol. 17, no. 11, p. 2032, Nov 1999. [Online]. Available: <http://jlt.osa.org/abstract.cfm?URI=jlt-17-11-2032>
- [40] T. Baba and M. Nakamura, “Photonic crystal light deflection devices using the superprism effect,” *Quantum Electronics, IEEE Journal of*, vol. 38, no. 7, pp. 909–914, Jul 2002.
- [41] S. Y. Lin, J. G. Fleming, D. L. Hetherington, B. K. Smith, R. Biswas, K. M. Ho, M. M. Sigalas, W. Zubrzycki, S. R. Kurtz, and J. Bur, “A three-dimensional photonic crystal operating at infrared wavelengths,” *Nature*, vol. 394, no. 6690, pp. 251–253, Jul 1998. [Online]. Available: <http://dx.doi.org/10.1038/28343>
- [42] S. Noda, K. Tomoda, N. Yamamoto, and A. Chutinan, “Full three-dimensional photonic bandgap crystals at near-infrared wavelengths,” *Science*, vol. 289, no. 5479, pp. 604–606, 2000. [Online]. Available: <http://science.sciencemag.org/content/289/5479/604>
- [43] J. D. Jackson, *Classical Electrodynamics*.
- [44] S. G. Johnson and J. D. Joannopoulos, “Block-iterative frequency-

- domain methods for maxwell's equations in a planewave basis," *Opt. Express*, vol. 8, no. 3, pp. 173–190, 2001. [Online]. Available: <http://www.opticsexpress.org/abstract.cfm?URI=OPEX-8-3-173>
- [45] B. Momeni and A. Adibi, "Systematic design of superprism-based photonic crystal demultiplexers," *Selected Areas in Communications, IEEE Journal on*, vol. 23, no. 7, pp. 1355 – 1364, july 2005.
- [46] B. Momeni, J. Huang, M. Soltani, M. Askari, S. Mohammadi, M. Rakhshandehroo, and A. Adibi, "Compact wavelength demultiplexing using focusing negative index photonic crystal superprisms," *Opt. Express*, vol. 14, no. 6, pp. 2413–2422, Mar 2006. [Online]. Available: <http://www.opticsexpress.org/abstract.cfm?URI=oe-14-6-2413>
- [47] B. E. Nelson, M. Gerken, D. A. B. Miller, R. Piestun, C.-C. Lin, and J. S. Harris, "Use of a dielectric stack as a one-dimensional photonic crystal for wavelength demultiplexing by beam shifting," *Opt. Lett.*, vol. 25, no. 20, pp. 1502–1504, Oct 2000. [Online]. Available: <http://ol.osa.org/abstract.cfm?URI=ol-25-20-1502>
- [48] D. Bernier, X. L. Roux, A. Lupu, D. Marris-Morini, L. Vivien, and E. Cassan, "Compact, low cross-talk cwdm demultiplexer using photonic crystal superprism," *Opt. Express*, vol. 16, no. 22, pp. 17 209–17 214, Oct 2008. [Online]. Available: <http://www.opticsexpress.org/abstract.cfm?URI=oe-16-22-17209>
- [49] B. Momeni and A. Adibi, "An approximate effective index model for efficient analysis and control of beam propagation effects in photonic crystals," *J.*

- Lightwave Technol.*, vol. 23, no. 3, p. 1522, Mar 2005. [Online]. Available: <http://jlt.osa.org/abstract.cfm?URI=jlt-23-3-1522>
- [50] E. Yablonovitch, T. J. Gmitter, R. D. Meade, A. M. Rappe, K. D. Brommer, and J. D. Joannopoulos, “Donor and acceptor modes in photonic band structure,” *Phys. Rev. Lett.*, vol. 67, pp. 3380–3383, Dec 1991. [Online]. Available: <https://link.aps.org/doi/10.1103/PhysRevLett.67.3380>
- [51] S. Noda, A. Chutinan, and M. Imada, “Trapping and emission of photons by a single defect in a photonic bandgap structure,” *Nature*, vol. 407, no. 6804, pp. 608–610, Oct 2000. [Online]. Available: <http://dx.doi.org/10.1038/35036532>
- [52] B.-S. Song, S. Noda, and T. Asano, “Photonic devices based on in-plane hetero photonic crystals,” *Science*, vol. 300, no. 5625, pp. 1537–1537, 2003. [Online]. Available: <http://science.sciencemag.org/content/300/5625/1537>
- [53] Y. Lai, S. Pirotta, G. Urbinati, D. Gerace, M. Minkov, V. Savona, A. Badolato, and M. Galli, “Genetically designed l3 photonic crystal nanocavities with measured quality factor exceeding one million,” *Applied Physics Letters*, vol. 104, no. 24, p. 241101, 2014. [Online]. Available: <http://dx.doi.org/10.1063/1.4882860>
- [54] Y. Akahane, T. Asano, B.-S. Song, and S. Noda, “High-q photonic nanocavity in a two-dimensional photonic crystal,” *Nature*, vol. 425, no. 6961, pp. 944–947, Oct 2003. [Online]. Available: <http://dx.doi.org/10.1038/nature02063>
- [55] A. Yariv, Y. Xu, R. K. Lee, and A. Scherer, “Coupled-resonator optical

- waveguide: a proposal and analysis,” *Opt. Lett.*, vol. 24, no. 11, pp. 711–713, Jun 1999. [Online]. Available: <http://ol.osa.org/abstract.cfm?URI=ol-24-11-711>
- [56] D. O’Brien, M. Settle, T. Karle, A. Michaeli, M. Salib, and T. Krauss, “Coupled photonic crystal heterostructure nanocavities,” *Opt. Express*, vol. 15, no. 3, pp. 1228–1233, Feb 2007. [Online]. Available: <http://www.opticsexpress.org/abstract.cfm?URI=oe-15-3-1228>
- [57] M. Notomi, E. Kuramochi, and T. Tanabe, “Large-scale arrays of ultrahigh-q coupled nanocavities,” *Nat Photon*, vol. 2, no. 12, pp. 741–747, Dec 2008. [Online]. Available: <http://dx.doi.org/10.1038/nphoton.2008.226>
- [58] R. W. Boyd, “Slow light, fast light, and backwards light: Fundamentals and applications,” in *Integrated Photonics and Nanophotonics Research and Applications / Slow and Fast Light*. Optical Society of America, 2007, p. SMA2. [Online]. Available: <http://www.osapublishing.org/abstract.cfm?URI=SL-2007-SMA2>
- [59] Z. Shi, R. W. Boyd, D. J. Gauthier, and C. C. Dudley, “Enhancing the spectral sensitivity of interferometers using slow-light media,” *Opt. Lett.*, vol. 32, no. 8, pp. 915–917, Apr 2007. [Online]. Available: <http://ol.osa.org/abstract.cfm?URI=ol-32-8-915>
- [60] Z. Shi, R. W. Boyd, R. M. Camacho, P. K. Vudyaasetu, and J. C. Howell, “Slow-light fourier transform interferometer,” *Phys. Rev. Lett.*, vol. 99, p. 240801, Dec 2007. [Online]. Available:

<https://link.aps.org/doi/10.1103/PhysRevLett.99.240801>

- [61] J. Wang, Y. Zhang, X. Zhang, H. Tian, H. Wu, Y. Cai, J. Zhang, and P. Yuan, “Enhancing the sensitivity of fiber mach–zehnder interferometers using slow and fast light,” *Opt. Lett.*, vol. 36, no. 16, pp. 3173–3175, Aug 2011. [Online]. Available: <http://ol.osa.org/abstract.cfm?URI=ol-36-16-3173>
- [62] D. Taillaert, H. Chong, P. I. Borel, L. H. Frandsen, R. M. D. L. Rue, and R. Baets, “A compact two-dimensional grating coupler used as a polarization splitter,” *IEEE Photonics Technology Letters*, vol. 15, no. 9, pp. 1249–1251, Sept 2003.
- [63] D. Taillaert, F. V. Laere, M. Ayre, W. Bogaerts, D. V. Thourhout, P. Bienstman, and R. Baets, “Grating couplers for coupling between optical fibers and nanophotonic waveguides,” *Japanese Journal of Applied Physics*, vol. 45, no. 8R, p. 6071, 2006. [Online]. Available: <http://stacks.iop.org/1347-4065/45/i=8R/a=6071>
- [64] T. Baba and T. Matsumoto, “Resolution of photonic crystal superprism,” *Appl. Phys. Lett.*, vol. 81, no. 13, pp. 2325–2327, 2002. [Online]. Available: <http://dx.doi.org/doi/10.1063/1.1508813>
- [65] A. F. Oskooi, D. Roundy, M. Ibanescu, P. Bermel, J. D. Joannopoulos, and S. G. Johnson, “MEEP: A flexible free-software package for electromagnetic simulations by the FDTD method,” *Computer Physics Communications*, vol. 181, pp. 687–702, January 2010.

- [66] J. Witzens, T. Baehr-Jones, and A. Scherer, “Hybrid superprism with low insertion losses and suppressed cross-talk,” *Phys. Rev. E*, vol. 71, p. 026604, Feb 2005. [Online]. Available: <http://link.aps.org/doi/10.1103/PhysRevE.71.026604>
- [67] S. Cheung, T. Su, K. Okamoto, and S. J. B. Yoo, “Ultra-compact silicon photonic 512 512 25 ghz arrayed waveguide grating router,” vol. 20, pp. 310–316, 07 2014.
- [68] A. V. Velasco, P. Cheben, P. J. Bock, A. Delâge, J. H. Schmid, J. Lapointe, S. Janz, M. L. Calvo, D.-X. Xu, M. Florjańczyk, and M. Vachon, “High-resolution fourier-transform spectrometer chip with microphotonic silicon spiral waveguides,” *Opt. Lett.*, vol. 38, no. 5, pp. 706–708, Mar 2013. [Online]. Available: <http://ol.osa.org/abstract.cfm?URI=ol-38-5-706>
- [69] X. Gan, N. Pervez, I. Kyymissis, F. Hatami, and D. Englund, “A high-resolution spectrometer based on a compact planar two dimensional photonic crystal cavity array,” *Applied Physics Letters*, vol. 100, no. 23, p. 231104, 2012.
- [70] B. Redding, S. F. Liew, R. Sarma, and H. Cao, “Compact spectrometer based on a disordered photonic chip,” *Nature Photonics*, vol. 7, no. 9, pp. 746–751, 2013.
- [71] P. B. Deotare, M. W. McCutcheon, I. W. Frank, M. Khan, and M. Lonar, “High quality factor photonic crystal nanobeam cavities,” *Applied Physics Letters*, vol. 94, no. 12, p. 121106, 2009. [Online]. Available: <http://dx.doi.org/10.1063/1.3107263>
- [72] M. Galli, S. Portalupi, M. Belotti, L. Andreani, L. O’Faolain, and T. Krauss, “Light scattering and fano resonances in high- Q photonic

- crystal nanocavities,” *Appl. Phys. Lett.*, vol. 94, no. 7, pp. 071101–071101, 2009.
- [73] B. Wild, R. Ferrini, R. Houdre, M. Mulot, S. Anand, and C. Smith, “Temperature tuning of the optical properties of planar photonic crystal microcavities,” *Applied physics letters*, vol. 84, no. 6, pp. 846–848, 2004.
- [74] S. L. Portalupi, M. Galli, M. Belotti, L. C. Andreani, T. F. Krauss, and L. O’Faolain, “Deliberate versus intrinsic disorder in photonic crystal nanocavities investigated by resonant light scattering,” *Physical Review B*, vol. 84, no. 4, p. 045423, 2011.
- [75] K. Hennessy, A. Badolato, A. Tamboli, P. Petroff, E. Hu, M. Atatüre, J. Dreiser, and A. Imamoğlu, “Tuning photonic crystal nanocavity modes by wet chemical digital etching,” *Applied Physics Letters*, vol. 87, no. 2, p. 021108, 2005.
- [76] A. Faraon, D. Englund, D. Bulla, B. Luther-Davies, B. J. Eggleton, N. Stoltz, P. Petroff, and J. Vučković, “Local tuning of photonic crystal cavities using chalcogenide glasses,” *Applied Physics Letters*, vol. 92, no. 4, p. 043123, 2008.
- [77] K. Hennessy, C. Högerle, E. Hu, A. Badolato, and A. Imamoğlu, “Tuning photonic nanocavities by atomic force microscope nano-oxidation,” *Applied physics letters*, vol. 89, no. 4, p. 041118, 2006.
- [78] H. Lee, S. Kiravittaya, S. Kumar, J. Plumhof, L. Balet, L. Li, M. Francardi, A. Gerardino, A. Fiore, A. Rastelli *et al.*, “Local tuning of photonic crystal nanocavity modes by laser-assisted oxidation,” *Applied Physics Letters*, vol. 95, no. 19, p. 191109, 2009.

- [79] C. J. Chen, J. Zheng, T. Gu, J. F. McMillan, M. Yu, G.-Q. Lo, D.-L. Kwong, and C. W. Wong, “Selective tuning of high-q silicon photonic crystal nanocavities via laser-assisted local oxidation,” *Optics express*, vol. 19, no. 13, pp. 12 480–12 489, 2011.
- [80] R. W. Boyd, “Material slow light and structural slow light: similarities and differences for nonlinear optics,” *J. Opt. Soc. Am. B*, vol. 28, no. 12, pp. A38–A44, Dec 2011. [Online]. Available: <http://josab.osa.org/abstract.cfm?URI=josab-28-12-A38>
- [81] T. Baba, “Slow light in photonic crystals,” *Nat Photon*, vol. 2, no. 8, pp. 465–473, Aug 2008. [Online]. Available: <http://dx.doi.org/10.1038/nphoton.2008.146>
- [82] T. F. Krauss, “Slow light in photonic crystal waveguides,” *Journal of Physics D: Applied Physics*, vol. 40, no. 9, p. 2666, 2007. [Online]. Available: <http://stacks.iop.org/0022-3727/40/i=9/a=S07>
- [83] J. Li, T. P. White, L. O’Faolain, A. Gomez-Iglesias, and T. F. Krauss, “Systematic design of flat band slow light in photonic crystal waveguides,” *Opt. Express*, vol. 16, no. 9, pp. 6227–6232, Apr 2008. [Online]. Available: <http://www.opticsexpress.org/abstract.cfm?URI=oe-16-9-6227>
- [84] K. M. Awan, S. A. Schulz, D. X. Liu, K. Dolgaleva, J. Upham, and R. W. Boyd, “Post-process wavelength tuning of silicon photonic crystal slow-light waveguides,” *Opt. Lett.*, vol. 40, no. 9, pp. 1952–1955, May 2015. [Online]. Available: <http://ol.osa.org/abstract.cfm?URI=ol-40-9-1952>

- [85] M. Minkov and V. Savona, “Wide-band slow light in compact photonic crystal coupled-cavity waveguides,” *Optica*, vol. 2, no. 7, pp. 631–634, Jul 2015. [Online]. Available: <http://www.osapublishing.org/optica/abstract.cfm?URI=optica-2-7-631>
- [86] A. Gomez-Iglesias, D. OBrien, L. OFaolain, A. Miller, and T. F. Krauss, “Direct measurement of the group index of photonic crystal waveguides via fourier transform spectral interferometry,” *Applied Physics Letters*, vol. 90, no. 26, p. 261107, 2007. [Online]. Available: <http://dx.doi.org/10.1063/1.2752761>
- [87] T. Baba and D. Ohsaki, “Interfaces of photonic crystals for high efficiency light transmission,” *Japanese Journal of Applied Physics*, vol. 40, no. 10R, p. 5920, 2001. [Online]. Available: <http://stacks.iop.org/1347-4065/40/i=10R/a=5920>
- [88] S. A. Kuchinsky, V. Y. Golyatin, and A. Y. Kutikov, “Coupling in pbg material with high group index,” pp. 59–70, 2003. [Online]. Available: <http://dx.doi.org/10.1117/12.479493>
- [89] B. Momeni and A. Adibi, “Adiabatic matching stage for coupling of light to extended bloch modes of photonic crystals,” *Applied Physics Letters*, vol. 87, no. 17, p. 171104, 2005. [Online]. Available: <http://dx.doi.org/10.1063/1.2115081>